

CHARTING THE INTERSTELLAR MAGNETIC FIELD CAUSING THE *INTERSTELLAR BOUNDARY EXPLORER (IBEX)* RIBBON OF ENERGETIC NEUTRAL ATOMS

P. C. FRISCH¹, A. BERDYUGIN², V. PIROLA², A. M. MAGALHAES³, D. B. SERIACOPI³, S. J. WIKTOROWICZ⁴, B-G ANDERSSON⁵,
H. O. FUNSTEN⁶, D. J. MCCOMAS^{7,12}, N. A. SCHWADRON⁸, J. D. SLAVIN⁹, A. J. HANSON¹⁰, AND C.-W. FU^{11,13}

¹Department of Astronomy and Astrophysics, University of Chicago, Chicago, IL 60637, USA

²Finnish Centre for Astronomy with ESO, University of Turku, Finland

³Inst. de Astronomia, Geofísica e Ciências Atmosféricas, Universidade de São Paulo, Brazil

⁴Department of Astronomy, University of California at Santa Cruz, Santa Cruz, CA, USA

⁵SOFIA Science Center, USRA, Moffett Field, CA, USA

⁶Los Alamos National Laboratory, Los Alamos, NM, USA

⁷Southwest Research Institute, San Antonio, TX, USA

⁸Space Science Center, University of New Hampshire, USA

⁹Harvard-Smithsonian Center for Astrophysics, Cambridge, MA, USA

¹⁰School of Informatics and Computing, Indiana University, Bloomington, IN, USA

¹¹School of Computer Engineering, Nanyang Technological University, Singapore

Received 2015 June 24; accepted 2015 October 19; published 2015 November 23

ABSTRACT

The interstellar magnetic field (ISMF) near the heliosphere is a fundamental component of the solar galactic environment that can only be studied using polarized starlight. The results of an ongoing survey of the linear polarizations of local stars are analyzed with the goal of linking the ISMF that shapes the heliosphere to the nearby field in interstellar space. We present new results on the direction of the magnetic field within 40 pc obtained from analyzing polarization data using a merit function that determines the field direction that provides the best fit to the polarization data. Multiple magnetic components are identified, including a dominant interstellar field, B_{POL} , that is aligned with the direction $l, b = 36^{\circ}.2, 49^{\circ}.0 (\pm 16^{\circ}.0)$. Stars tracing B_{POL} have the same mean distance as stars that do not trace B_{POL} , but show weaker average polarizations consistent with a smaller column density of polarizing material. B_{POL} is aligned with the ISMF traced by the IBEX Ribbon to within $7.6_{-7.6}^{+14.9}$ degrees. The variations in the polarization position angle directions derived from the data that best match B_{POL} indicate a low level of magnetic turbulence, $\sim 9^{\circ} \pm 1^{\circ}$. The direction of B_{POL} is obtained after excluding polarization data tracing a separate magnetic structure that appears to be associated with interstellar dust deflected around the heliosphere. The velocities of local interstellar clouds relative to the Local Standard of Rest (LSR) increase with the angles between the LSR velocities and B_{POL} , indicating that the kinematics of local interstellar material is ordered by the ISMF. The Loop I superbubble that extends close to the Sun contains dust that reddens starlight and whose distance is determined by the color excess $E(B - V)$ of starlight. Polarizations caused by grains aligned with respect to B_{POL} are consistent with the location of the Sun in the rim of the Loop I superbubble. An angle of $76.8_{-27.6}^{+23.5}$ between B_{POL} and the bulk LSR velocity the local interstellar material indicates a geometry that is consistent with an expanding superbubble. The efficiency of grain alignment in the local interstellar medium has been assessed using stars where both polarization data and hydrogen column density data are available. Nearby stars appear to have larger polarizations than expected based on reddened sightlines, which is consistent with previous results, but uncertainties are large. Optical polarization and color excess $E(B - V)$ data indicate the presence of nearby interstellar dust in the BICEP2 field. Color excess $E(B - V)$ indicates an optical extinction of $A_V > 0.6$ in the BICEP2 field, while the polarization data indicate that $A_V > 0.09$ mag. The IBEX Ribbon ISMF extends to the boundaries of the BICEP2 region.

Key words: dust, extinction – ISM: clouds – ISM: magnetic fields – polarization – Sun: heliosphere

1. INTRODUCTION

The Sun is traveling through a dynamically evolving interstellar environment that contains low density, magnetized, partially ionized interstellar material traveling rapidly away from the center of the Loop I superbubble. The heliosphere is shaped by the solar wind interaction with the interstellar gas and magnetic field. A unique diagnostic of the direction of the magnetic field at the heliosphere location is provided by the Ribbon of energetic neutral atoms (ENAs) discovered by the *Interstellar Boundary Explorer (IBEX)* (Funsten et al.

2009, 2013; McComas et al. 2009; Schwadron et al. 2009, 2011). The flux of TeV galactic cosmic rays at the Earth is controlled by the ISMF direction that is traced by the *IBEX* Ribbon (Schwadron et al. 2014). Similarly, galactic cosmic ray fluxes onto exoplanets and their astrospheres (stellar wind bubbles) depend on the interstellar magnetic field (ISMF) that surrounds the exoplanet system (Frisch 1993). Understanding the role of the ISMF in the past and future galactic environments of the solar system and nearby exoplanet systems requires knowledge of the magnetic field configuration and its connection to the magnetized and partially ionized medium in the galactic neighborhood of the heliosphere. The purpose of this study is to connect the ISMF that shapes the heliosphere with the extended magnetic field in the nearby interstellar clouds.

¹² Also University of Texas, San Antonio, TX, USA.

¹³ After December 2015 at Chinese University of Hong Kong, Hong Kong China.

Studies over the past century of optical and ultraviolet (UV) interstellar absorption lines, and the reddening of starlight by interstellar dust, have revealed the physical properties, dynamics and distribution of local interstellar material within 40 pc of the Sun (Frisch et al. 2011). Although the Sun was known to be located in a region of very low interstellar dust densities (Fitzgerald 1968), measurements of polarized starlight proved to be a viable method for testing the very local ISMF (Piirola 1977; Tinbergen 1982). Nevertheless, the interstellar dust content and magnetic field configuration close to the heliosphere have been enigmatic. In this paper we present new high-sensitivity measurements of polarized starlight that allow filling the gaps in our knowledge of the configuration of the local ISMF within 40 pc of the Sun.

Polarized starlight provides the only method for tracing the ISMF direction in the low density interstellar medium (ISM) near the solar system. For polarization due to dichroic extinction, starlight becomes linearly polarized while traversing a medium formed by charged asymmetric submicron-sized interstellar dust grains that are aligned with the most opaque grain axis oriented perpendicular to the ISMF (Hoang & Lazarian 2014). Comparisons between polarized dust emission, polarized synchrotron emission, and linearly polarized optical starlight indicate that optical polarization position angles are oriented parallel to the ISMF direction in the nearby ISM (Frisch et al. 2015b). The low interstellar column densities near the Sun (Bohlin et al. 1978; Frisch & York 1983; Wood et al. 2005) impose two conditions on the study of the local ISMF: high-sensitivity polarization measurements are required, and the analysis method must utilize statistically weighted data so that low-significance polarization data can be included.

The goal of charting the direction of the ISMF within 40 pc is to relate the interstellar field in the solar neighborhood to the ISMF around the heliosphere. In Frisch et al. (2010a, Paper I) we derived the orientation of the local ISMF by assuming that the field has a dipole configuration, and that the pole of this field could be retrieved by applying a minimization algorithm to the polarization position angles. The analysis was based on polarization data in the literature. New data were collected on the polarizations of nearby stars in order to fully constrain the magnetic field direction (Frisch et al. 2012, Paper II). Applying a minimization procedure with statistically weighted position angles, to the extended data set produced a interstellar field direction close to the direction of the *IBEX* Ribbon ISMF. The two directions were within $\sim 33^\circ \pm 27^\circ$ of each other. The velocity vector of the bulk flow of the cluster of local interstellar clouds (CLIC) relative to the Local Standard of Rest (LSR) was found to form an angle of $\sim 76^\circ$ with the best-fitting ISMF to the polarization data. Subsequently, we identified a distinct nearby magnetic structure that appears to be formed by aligned dust grains entrained in the ISMF draping over the heliosphere (Frisch et al. 2015a).

The present study includes new data that have been collected in both the northern and southern hemispheres in order to map the magnetic field in nearby interstellar space, described in Section 2. We refine the analysis method used in Papers I and II where a merit function is used to establish the best-fitting ISMF direction to the ensemble of interstellar polarization measurements (Section 3). The best-fitting ISMF direction to all qualifying polarization data is given in Section 4.1. Polarization data associated with a distinct filamentary polarization structure are identified (Section 4.2). Omission of the filament stars from

the data sample gives a best-fitting ISMF direction in close agreement with the *IBEX* ISMF direction (Section 4.3) although not all significant polarizations agree (Section 4.4). Magnetic turbulence is estimated from the dispersion of polarization position angles (Section 4.5). Additional possible unrecognized local ISMF components are briefly considered (Section 4.6). The broad implications of these results are discussed in Section 5, including the relation between B_{POL} and the *IBEX* Ribbon (Section 5.1), galactic cosmic ray asymmetries (Section 5.2), the origin of the separate polarization filament (Section 5.3), the gas–dust relationship (Section 5.4), and local interstellar clouds and the Loop I superbubble (Section 5.5). The polarization data show that nearby low-extinction interstellar dust, and magnetic fields, are found in the BICEP2 region of study (Section 5.6). Conclusions are presented in Section 6. Appendices provide additional details on the stars with polarization position angles that best match the *IBEX* ISMF direction that traces the LIC field (Appendix A), the source of the color excess data (Appendix B), the formulae that characterize the efficiency of polarization mechanisms (Appendix C), and the conversion of heliocentric velocities to the LSR for the purpose of comparing the cloud velocity with the ISMF direction (Appendix D). As an aside, it is found that the contemporary solar apex motion is similar to that found by Herschel (1783, Appendix D).

2. POLARIZATION DATA USED TO DETERMINE THE MAGNETIC FIELD DIRECTION

Starlight polarization attributed to interstellar dust aligned with respect to the magnetic field was discovered in 1949 (see Andersson 2015, for a review). Multiple measurements of starlight polarized in the ISM were acquired during the last half of the 20th century, and later assembled into a single catalog (Heiles 2000). The 20th century data sets used in this analysis included the discovery of the ISMF within 40 pc of the Sun in the fourth galactic quadrant ($\ell = 270^\circ\text{--}360^\circ$, Piirola 1977; Tinbergen 1982). More recently, high sensitivity polarimeters capable of 3σ detections of polarization strengths $<0.01\%$ have become available (Pereyra & Magalhães 2007; Wisniewski et al. 2007; Bailey et al. 2010, 2015; Berdyugin et al. 2014; Piirola et al. 2014; Wiktorowicz & Nofi 2015; Wiktorowicz et al. 2015).

Modern polarimeters are capable of detecting interstellar polarizations in the low column density nearby clouds. Surveys of interstellar polarizations indicate that, in the absence of line-of-sight depolarization, polarization strengths and extinction are related (Serkowski et al. 1975; Fosalba et al. 2002, Section 5.4, Appendix C). A heuristic relation corresponding to the upper envelope of the distribution of polarization strength as a function of color-excess $E(B - V)$ provides a nominal upper-limit for expected polarizations. For the low column densities of the ISM within 25 pc, $N(\text{H}^\circ) < 10^{18.7}$ (Wood et al. 2005), polarizations of up to $\sim 0.014\%$ are expected (see the discussion of the relation between $E(B - V)$, polarization strengths, and $N(\text{H})$ in Appendix C). Modern polarimeters are therefore capable of mapping the direction of the local ISMF.

In this paper we utilize new polarization measurements that have been acquired with the DiPol2 polarimeter at the KVA telescope in La Palma, Canary Islands (Berdyugin et al. 2014), the IAGPOL polarimeter at the LNA at Picos dos Dios in Brazil (Pereyra & Magalhães 2007; Wisniewski et al. 2007), and the POLISH2 polarimeter at the Lick Observatory in

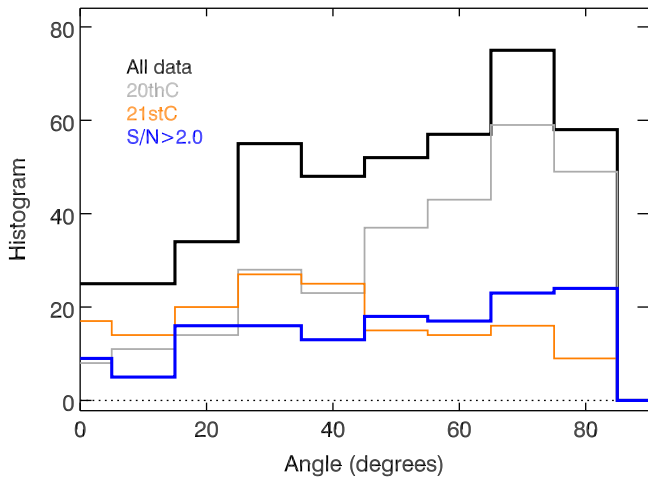


Figure 1. Angular distribution of stars with respect to heliosphere nose direction. The number of stars in the designated category is plotted against the angle between the star and the heliosphere nose. The thin gray and orange lines represent data collected in the 20th and 21st centuries, respectively. The smaller number of 21st century targets at large angles from the heliosphere nose, compared to the same numbers for 20th century stars, is partly due to choices made in the selection of the target stars (Table 2). The black line shows the total data set. The blue line shows the subsample with $P/\Delta P \geq 2.0$.

California (Wiktorowicz & Nofi 2015; Wiktorowicz et al. 2015). These data include measurements with 3σ sensitivities of 0.01% or better. Data on the polarizations of nearby stars from the high-sensitivity survey with the PlanetPol instrument (Bailey et al. 2010), the Loop I polarization survey of Santos et al. (2011), and the Heiles (2000) polarization catalog are also incorporated into the polarization database used in this study.

The region of study in this paper is restricted to stars within 90° of the heliosphere nose since this interval includes the patch of nearby polarizing dust grains found by Tinbergen (1982), it includes the region of right ascension R.A. > 17 HR where Bailey et al. (2010) have shown that polarization strengths increase with distance, and it contains the *IBEX* Ribbon (Section 1). This region also includes the star α Oph (14 pc) with striking properties for the foreground ISM (Munch & Unsold 1962; Frisch 1981; Frisch et al. 1987). The angular constraint that program stars must be located within 90° of the heliosphere nose effectively restricts stars to the galactic center hemisphere, but includes stars at high-latitudes.

These combined data form a heterogeneous set of over 700 measurements of polarizations for 520 stars within 40 pc. Over three hundred of these stars are within 90° of the direction of the heliosphere nose, $\ell, b = 3^\circ.2, 15^\circ.5$ (e.g., McComas et al. 2015). Figure 1 histograms the distribution of the angles between the measurements in the database and the heliosphere nose as a function of the significance of the polarization measurement and the epoch of measurement. Thirty percent of these stars within 40 pc have polarizations that have been measured at a significance of $P/\Delta P \geq 2.0$, where P and ΔP are polarization and the mean error of the polarization. The merit function that we have developed to assess the best-fitting ISMF direction to these polarization data includes a weighting factor that allows the use of measurements at all levels of $P/\Delta P$ in this analysis so that weaker polarizations are useful data points (Section 3). The data from the 20th century provide an unbiased spatial sampling of the magnetic field (thin gray line

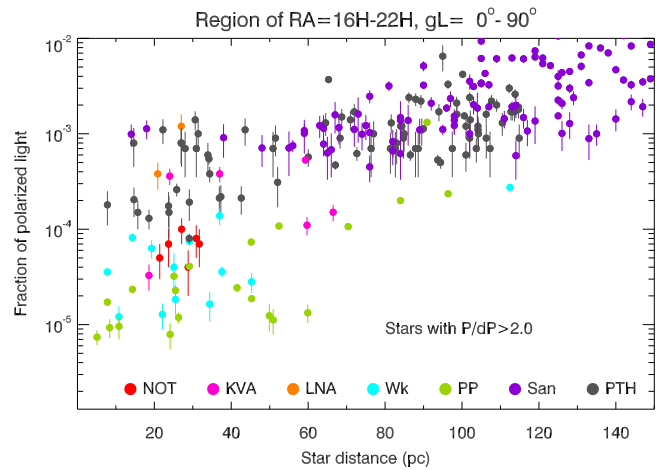


Figure 2. Polarization strengths vs. distance. The fractional linear polarizations of the E -component of starlight is plotted for stars in the first galactic quadrant, $\ell = 0^\circ$ – 90° , between R.A. 17 HR and 22 HR, and where $P/\Delta P > 2.0$. The general increase of polarization strengths with distance becomes less obvious near the Sun where clumping of gas and dust becomes evident, and systematic differences due to instrumental sensitivities are relatively more important. These data create a heterogeneous set collected using polarimeters with different bandpasses and sensitivity levels. Color coding denotes the data source: KVA (red), NOT (pink, Paper II), 20th century data (PTH, gray, Pirola 1977; Tinbergen 1982; Heiles 2000), LNA (orange), Lick (Wk, turquoise, Wiktorowicz et al. 2015), PlanetPol (green, Bailey et al. 2010), and (San, Santos et al. 2011, purple). The distance uncertainties (not shown) are typically less than 4% of the star distances.

in Figure 1), whereas many of the 21st century data were collected specifically for this project and were selected by their proximity to the heliosphere nose.

Polarizations are plotted against the star distance in Figure 2 for those stars that are located between R.A. = 17 H and R.A. = 22 H in the first galactic quadrant, $\ell = 0^\circ$ – 90° . Bailey et al. (2010) showed that the strengths of polarizations in this region increase with distance (also see Figure 7 in Paper II), and we have shown that this increase is consistent with a dust bridge reaching from the solar vicinity out to the North Polar Spur region (Frisch et al. 2015b).

The search for the ISMF direction that best matches these polarization data uses polarization position angles, θ_{PA} , and not polarization strengths (Section 3). Polarization position angles that trace a single magnetic field direction are independent of the wavelength of the measurement and therefore provide a consistently defined quantity for data collected at different sensitivities using different spectral bands. In addition, the size distributions of the polarizing grains are poorly known. In situ measurements of interstellar dust grains by *Ulysses* and other spacecraft show that the size range extends from ~ 0.04 to $2.0 \mu\text{m}$ if the grains are compact silicates (Frisch et al. 1999; Landgraf et al. 2000; Krueger et al. 2015; Sterken et al. 2015). Since the wavelength of maximum polarization strengths depend on grain sizes, composition, and porosity (Serkowski et al. 1975; Andersson & Potter 2006; Andersson 2015), the polarization strengths can not be compared because of the different spectral bands of the various data sets.

The polarization position angles of the data assembled for this analysis are mapped in Figure 3. The uncertainties on the polarization position angles, $\arctan(\Delta P/2P)$ where ΔP is the uncertainty on the polarization strength, are plotted with “fan-shaped” symbols. The angular width of the fan indicates the uncertainty on the polarization position angle. The dots show

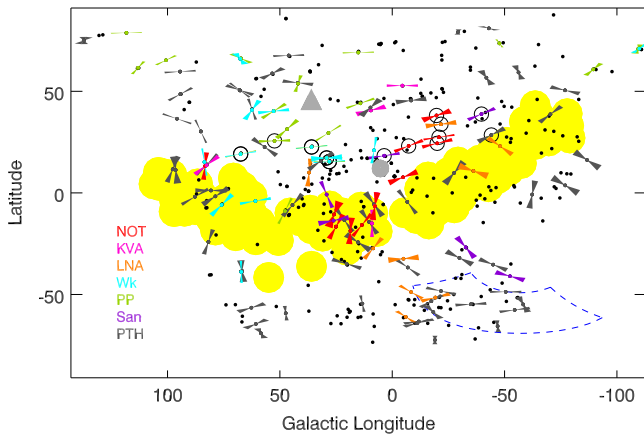


Figure 3. Polarization position angles for stars with $P/\Delta P > 2.0$ and within 40 pc and 90° of the heliosphere nose are plotted. The fan-shaped polygons indicate the angular uncertainty of the polarization position angles $\Delta\theta$. Stars with $P/\Delta P < 2\sigma$ are plotted with dots. The regions of the highest fluxes of 1 keV ENAs, corresponding to the *IBEX* Ribbon, are denoted in yellow. Circled stars indicate stars that trace the polarization filament (Sections 4.2, 5.3, Frisch et al. 2015a). The directions of the best-fitting ISMF B_{POL} and heliosphere nose are shown as gray triangles and dots, respectively. The dashed lines enclose the region observed by BICEP for CMB B-mode polarization (Section 5.6). Color coding of the polarizations indicate the data source (see Figure 2).

stars where $P/\Delta P < 2.0$. A nominal limit of $P/\Delta P = 2.0$ is used for plotting position angles since interstellar polarizations of stars within 40 pc tend to be weak with fewer stars showing $P/\Delta P > 3$. The analysis (Section 3) incorporates data with all uncertainty levels using the appropriate weighting factor. Since the mean errors of the polarizations from the different data sets vary, it is possible to have two measurements of the same star, corresponding to two adjacent data points in Figure 3, that show different mean errors. With only a few exceptions, these types of adjacent points do not represent discrepancies but rather result from the use of early polarization data with large uncertainties. Generally all measurements of a star are included with the use of weighted data points, with the exception of a few older data points that are clearly superseded by more accurate recent data. The circled stars in Figure 3 show the locations of the stars that trace a separate nearby magnetic structure, or “filament” (Sections 4.2, 5.3, Frisch et al. 2015a). The filament runs roughly parallel to the northern border of the *IBEX* Ribbon of ENAs (McComas et al. 2009; Schwadron et al. 2011), the brightest parts of which are plotted in yellow.

The data used in this paper differ from that of Paper II in that this analysis utilizes new observations from the LNA and KVA observatories (Table 2), and Lick Observatory (Wiktorowicz et al. 2015), and excludes otherwise qualifying Heiles data if later higher-quality data are also available.

3. MERIT FUNCTION FOR DERIVING THE ISMF DIRECTION FROM POLARIZATION DATA

Due to the low extinction of the nearby ISM where interstellar polarization strengths are weak, we have developed a method for combining weighted polarization data to evaluate the best-fitting ISMF direction to those data, utilizing all data including where $P/\Delta P < 2.0$. The strategy is to search for a regular dipole-like component to the ISMF that best matches the total group of polarization position angles indicated by the polarization data. A merit function describes how well the

polarization position angles are aligned with the field direction. It is evaluated for each possible ISMF direction to find the minimum value that provides the best-fitting ISMF direction for the polarization data set.

The merit function utilizes the fact that for linearly polarized starlight aligned with the direction of the ISMF in the diffuse ISM the sine of the polarization position angle¹⁴ will be zero in a coordinate system that is aligned with the ISMF poles. In Papers I and II, and here, the star sample is restricted to stars within 40 pc and 90° of the heliosphere nose. The same strategy of minimizing the sine of polarization position angles to evaluate the local ISMF direction is used also, where all possible ISMF directions are tested in order to determine the ISMF direction. In Paper I the data sample was restricted to $P/\Delta P > 2.5$ (where the polarization is P and the mean error of the measurement is ΔP). The limit of $P/\Delta P > 2.5$ resulted in the omission of a large amount of useful data. In Paper II, using a larger set of data that included new measurements, weighting was introduced into the merit function that tested for the best ISMF direction, so that data points with low statistical significance could still be incorporated into the analysis.

This use of a weighting function is continued in the present analysis. The weighting function is based on the bivariate statistical description of polarization position angles given in Naghizadeh-Khouei & Clarke (1993, NKC). This probability distribution accounts for the fact that while the polarizations are always positive, the underlying Stokes parameters can be either positive or negative. The outcome of using the NKC weighting function is that the statistical likeliness of position angles in the wings of the distribution are increased over the expectation of a true Gaussian distribution, and this property increases the value of incorporating polarizations with $P/\Delta P < 2.0$ into the analysis. Above $P/\Delta P = 6$ the probability distribution for polarization position angles reverts to a Gaussian.

The merit function $F_{\text{II}}(B_i)$ that tests for the ISMF direction that best describes the ensemble of polarization position angles, then becomes a combination of the requirement that the mean sine of the position angle is minimized and the statistical weighting of polarization position angles is maximized:

$$F_{\text{II}}(B_i) = N^{-1} \sum_{n=1}^N f_n(B_i) \quad \text{where } f_n(B_i) = \left| \frac{\sin(\theta_n(B_i))}{G_n} \right|. \quad (1)$$

The contribution of each individual star n to $F_{\text{II}}(B_i)$, for ISMF direction B_i , is $f_n(B_i)$. The quantity $\theta_n(B_i)$ is the polarization position angle $\theta_{\text{PA},n}$ for star n , which is calculated with respect to the i th possible ISMF direction B_i . The sum is over N stars. G_n (Equation (2)) is the NKC weighting factor for each star:

$$G_n(\theta_{\text{obs}}; \theta_o, P_o) = \frac{1}{\sqrt{\pi}} \left\{ \frac{1}{\sqrt{\pi}} + \eta_o \exp(\eta_o^2) \times [1 + \text{erf}(\eta_o)] \right\} \exp\left(-\frac{P_o^2}{2}\right) \quad (2)$$

¹⁴ The polarization position angle is defined as the angle between the linear polarization vector and a north-south meridian passing through the star, with values in the interval 0° and 180° and increasing toward the east.

for observed position angle θ_{obs} , “true” position angle θ_o , $P_o = \frac{P_{\text{true}}}{\sigma}$, mean error $\sigma = dP$, $\eta_o = \frac{P_o}{\sqrt{2}} \cos [2(\theta_{\text{obs}} - \theta_o)]$, and the Gaussian error function $\text{erf}(Z) = \frac{2}{\sqrt{\pi}} \int_0^Z \exp(-t^2) dt$.

Two limits were imposed in order to prevent unrecognized properties of the data from biasing the result. The value of G_n was capped at 3.5 in the analysis program to prevent overweighting any single star in the analysis. By use of this cap, the effects of possibly unrecognized intrinsically polarized stars, or any single data set with systematically smaller mean errors (e.g., the PlanetPol data), are minimized. A second limit was imposed by requiring G_n to be 1×10^{-5} or larger. Experience showed that weights below this level represent insignificant data points, but potentially cause numerical problems in the code. Note that polarization strengths are not used in this analysis because of the diversity of spectral bands with which these data were acquired (Section 2).

The possible directions for the ISMF pole, B_i , are then tested over a grid of one-degree intervals on the sky. For the best comparison between the interstellar polarization data and the ISMF traced by the *IBEX* Ribbon, only stars within 40 pc of the solar system and 90° of the heliosphere nose are included in the evaluation. The ISMF direction determined from all qualifying data is denoted B_{ALL} (see Section 4.1).

The function $F_{\text{II}}(B_i)$ does not incorporate the variance of the array being minimized. We have therefore also tested a merit function with the additional term, $\sigma(F_{\text{II}}(B_i))$, corresponding to the standard deviation of the array $F_{\text{II}}(B_i)$, for the function that is being minimized:

$$F_{\text{III}}(B_i) = F_{\text{II}}(B_i) \times \sigma(F_{\text{II}}(B_i)). \quad (3)$$

We make the assumption that if the method for determining the ISMF direction is to yield a robust result, then the directions found from Equations (1) and (3) must be similar. This condition is satisfied. The use of Equation (3) does increase the spatial gradients of the merit function, affecting the uncertainties of the B_{ALL} . Results from Equation (3) are not used to determine the best-fitting ISMF to these polarization data.

4. DIRECTION OF ISMF WITHIN 40 PC

4.1. Best-fitting Local Magnetic Field Direction to All Data

The simplest approximation is to assume that there is a single ISMF that controls the optical interstellar polarizations for stars within 40 pc and 90° of the heliosphere nose, as was also assumed in Papers I and II. All of the qualifying observations are used in the evaluations of the ISMF direction, except for the 20th century data collected in the Heiles (2000) catalog where observations range in precision levels. Those data are not used if a more recent, and presumably more precise, measurement is available for the same star. Justification for the approximation of a single field direction is provided by the low column densities, $N(\text{H}^\circ) < 10^{18.7}$, of the ISM within ~ 25 pc (e.g., Wood et al. 2005), and the fact that local clouds flow through space with roughly similar velocity vectors in the LSR, suggesting a common origin for the clouds (Frisch et al. 2002, 2011). It is shown below, however, that multiple magnetic structures appear to be present.

Analyzing the qualifying set of polarization data (Section 2), with the merit function $F_{\text{II}}(B_i)$ (Equation (1)) based on

weighted data points (Equation (2)), gives a best-fitting ISMF direction that is toward the direction $\ell = 16^\circ.3$, $b = 27^\circ.0$ (Figure 4, left). The uncertainty on this direction is determined by the width of the minimum of $F_{\text{II}}(B_i)$. Figure 5, left, shows the value of $F_{\text{II}}(B_i)$ plotted against the angle from this best-fitting ISMF direction for each location in the sky. The uncertainty on the best-fitting ISMF direction is assumed to be the angle that clearly distinguishes the minimum of $F_{\text{II}}(B_i)$ from an adjacent secondary minimum, or $\pm 15^\circ \text{ cm}^{-2}$. This new best-fitting direction differs by $27^\circ.6 \pm 29^\circ.2$ from the result of Paper II, which is not a significant difference. A test was also made to determine whether the use of $F_{\text{III}}(B_i)$ changed the best-fitting ISMF direction from these data, and it gave a similar direction directed toward $\ell = 15^\circ.3$, $b = 27^\circ.0$.

4.2. Identifying a Filamentary-shaped Magnetic Structure

As the sky coverage of the underlying polarization data set improves, it becomes more likely that inhomogeneities in the direction of the local ISMF will be sampled. Since the purpose of this study is to connect the ISMF that shapes the heliosphere with the local interstellar field, the analysis of the best-fitting ISMF to the polarization data needs to take into account the possibility there are multiple local ordered components of the magnetic field, so that polarizations clearly associated with a magnetic field that is different from the one that shapes the heliosphere can be omitted from the fits. In this section we identify a clearly identifiable secondary magnetic structure. The properties of this filament suggest that it is related to interstellar dust grains deflected around the heliosphere (Frisch et al. 2015a). In this section we justify the selection of these polarizations as belonging to a separate magnetic structure, and in the following section the magnetic field direction in the local ISM is evaluated for a data set that omits data that trace the polarization filament.

Using data from the PlanetPol polarimeter, Bailey et al. (2010) showed that the polarization strengths for stars in the region R.A. $> 17\text{H}$ increase with the distance of the target star. In Paper II we showed that the stars that formed the upper envelope in the polarization versus distance relation for this subset of the PlanetPol data contains a group of stars within 40 pc that traces a magnetic structure with an ordered ISMF direction that extends to within 10 pc of the Sun. In Paper II, this ordered field was characterized by a position angle gradient of $\text{PA}_{\text{R.A.}}$ of $\sim -0^\circ.25 \text{ pc}^{-1}$ (based on the fit $\theta_{\text{R.A.}} = 36.0(\pm 1.4) - 0.25(\pm 0.03)D$ for distance D and position angles expressed in the equatorial coordinate system, $\theta_{\text{R.A.}}$, e.g., with respect to R.A.).

Given this evidence for a magnetic structure suggested by the upper envelope to the polarization versus distance relation for the PlanetPol data, we have searched for additional stars within 40 pc in this spatial interval that might also show polarization position angles that vary systematically with distance indicating an ordered magnetic field. A total of thirteen stars (HD 131977, HD 161797, HD 120467, HIP 82283, HD 119756, HD 144253, HD 130819, HD 161096, HD 134987, HD 136894) were identified in the current data set by a systematic decrease of θ_{gal} with distance (see below). The stars tracing the magnetic structure are located between 6 pc and 29 pc from the Sun and appear to form an elongated feature spanning an angle of $\sim 5^\circ \times 98^\circ$, where the polarization position angles are parallel to the axis of the structure (see the

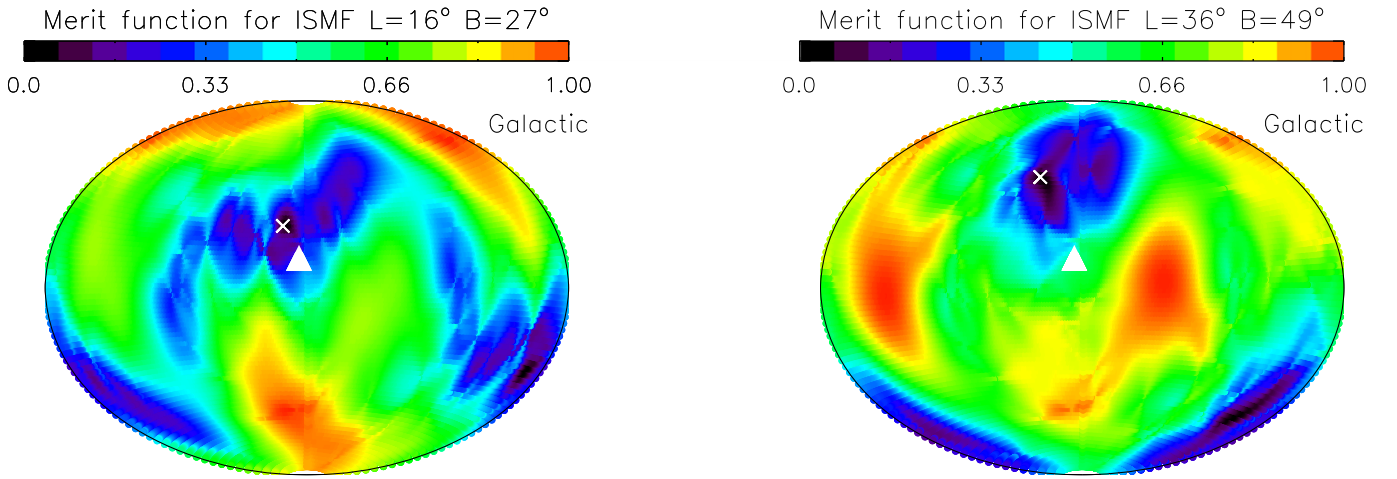


Figure 4. Values of the merit function, $F_{II}(B_i)$ for each location on the sky. $F_{II}(B_i)$ is normalized to the minimum value that gives the best-fitting ISMF direction. The color scale is based on a log scale. Left: the merit function for the fit to Equation (1) that utilizes all qualifying polarization measurements. The best-fitting ISMF direction for this star sample, B_{ALL} , is toward $\ell, b = 16^\circ 3, 27^\circ 0$. Right: the merit function calculated by omitting the filament stars from the fitted sample. The best-fitting ISMF without the filament stars, B_{POL} , is toward $\ell = 36^\circ 2, b = 49^\circ 0$. The location of the minimum of $F_{II}(B_i)$, is plotted with an “X,” and the heliosphere nose is located at the triangle. Uncertainties on these directions are shown in Figure 5 and listed in Table 1. The figures are centered on the galactic center, with galactic longitude increasing toward the left and latitude increasing toward the top.

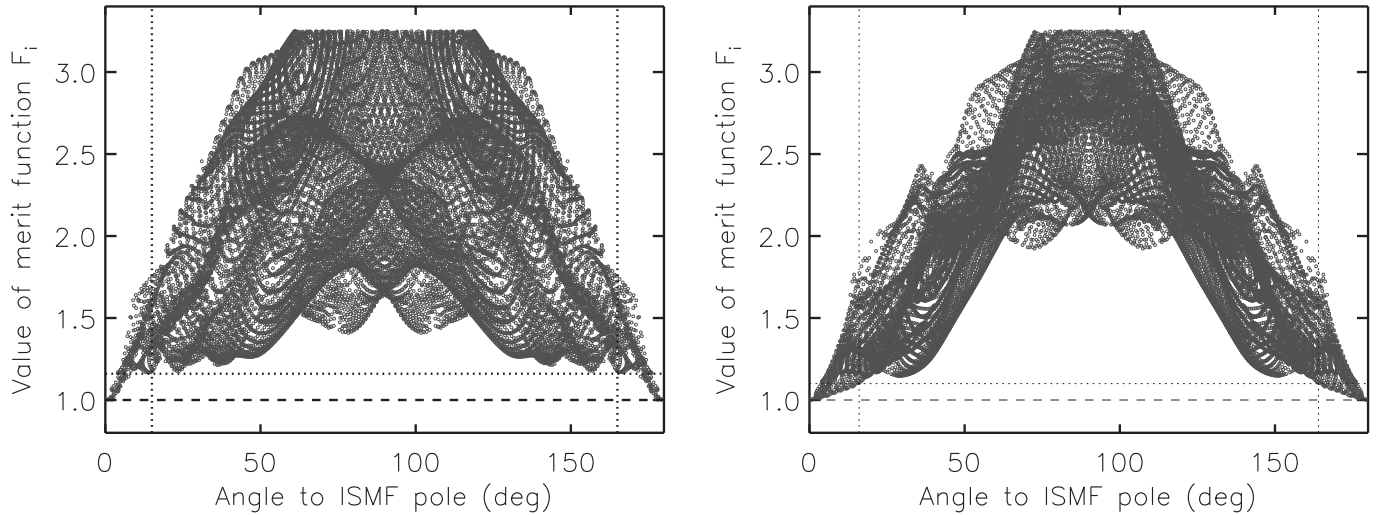


Figure 5. Uncertainties on the best-fitting ISMF direction for B_{ALL} (left) and B_{POL} (right). The uncertainties are given by the angular distribution normalized merit function $F_{II}(B_i)$ values (vertical axis), which are plotted against the angle between the best-fitting ISMF direction and the merit function at each point on the sky (horizontal axis). By definition, the merit function minimum is located at the position of the best-fitting ISMF. For B_{ALL} the uncertainties on the best-fitting ISMF are defined as the first minimum in the merit function array at $\pm 15^\circ$ (vertical dotted line, left figure). For B_{POL} , the uncertainty is arbitrarily assigned to the angle where the merit function is 10% above the best-fitting value, or $\pm 16^\circ$. The values of $f_n(B_i)$ for the star sample with the filament stars omitted (right) has a more compact angular distribution and is better defined than the function that includes the entire polarization data set (left, see Figure 4).

polarization data points that are circled in Figure 3). The geometric configuration of this structure is filamentary or edge-on. Since a filament would occupy the smallest volume of space, we suggest that it is filamentary.

The gradient in θ_{gal} with distance is quantified by dividing the thirteen stars into two separate groups and performing a linear fit to the variation of polarization versus distance for each group of stars. A slightly different slope of the θ_{PA} versus distance relationship was obtained for the two groups (Figure 6). The most slowly varying ISMF component is traced by seven stars and includes the original three PlanetPol stars from Paper II. The linear fit to θ_{PA} versus distance for the first set gives $\theta_{gal} = 106.8 (\pm 1.5) - 0.53 (\pm 0.08) D_{star}$, with a reduced χ^2 of 1.217 (lower group of stars in Figure 6). The second set of six stars in the same extended filamentary-shaped

feature can be fit by the line $\theta_{gal} = 130.0 (\pm 15.2) - 0.68 (\pm 0.65) D_{star}$, with a reduced χ^2 of 0.528 (upper group of stars in Figure 6). More than thirteen data points are plotted in Figure 6 because several of these stars have been observed multiple times.

The angle found in Paper II for the rotation of polarization position angles with distance was $\sim -0.25 \text{ pc}^{-1}$ for position angles presented in the equatorial coordinate system, whereas the slopes in the galactic coordinate system are -0.53 to -0.68 pc^{-1} , and the stars span an angular range of $\sim 98^\circ$ (Section 4.2). The factor of at least two difference between the slopes suggests that neither the galactic coordinate system nor the equatorial coordinate system is the correct system for evaluating the characteristics of the magnetic structure traced by the filament stars. It appears as if some of the variation of

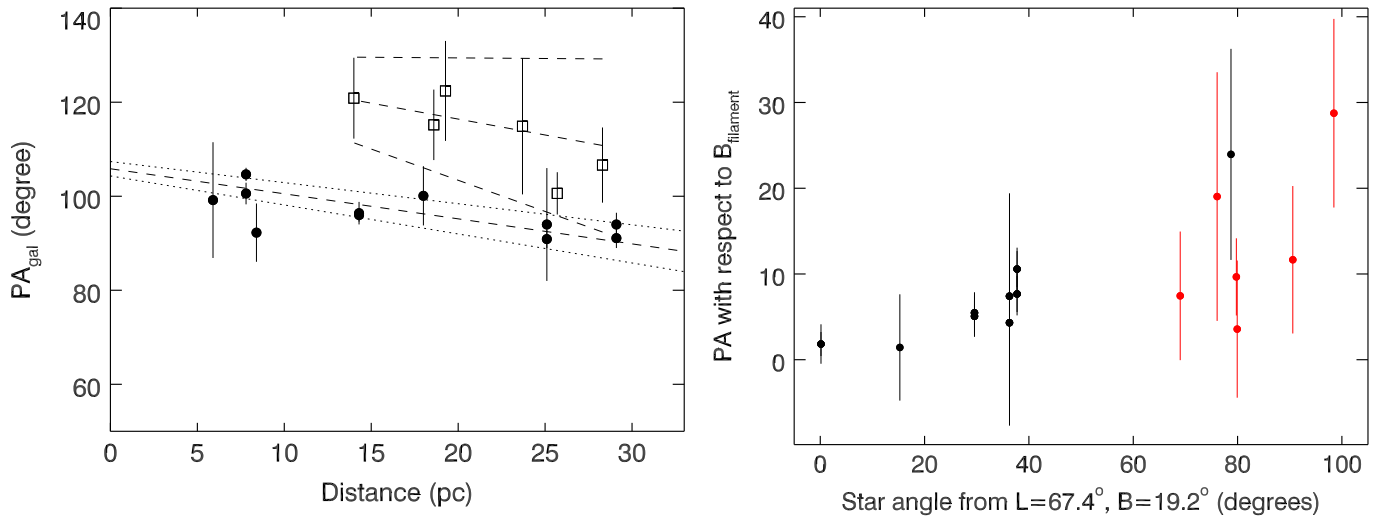


Figure 6. Left: galactic polarization position angles are plotted against the star distance for the two sets of stars that make up the magnetic “filament” feature (Section 4.2). Both sets of stars show polarization position angles expressed in galactic coordinates, θ_{gal} , that rotate with the distance of the star. The separate linear fits performed to the two subsets of stars in this filament are shown, together with the 1σ uncertainty of the fits. Right: the polarization position angles (vertical axis) are plotted against the angular distance from the star HD 172167 that is located at the end of the filament (horizontal axis). The position angles are expressed relative to the direction of the ISMF that provides the best fit to the filament polarizations, B_{FIL} . The ISMF derived from filament polarizations provides a more uniform description of the polarization position angles than does the north galactic pole.

the polarization position angle with distance is, instead, due to the rotation of the coordinate systems over the angular interval spanned by the star positions.

To remove this bias introduced by the coordinate system, we have applied the analysis method of Section 3 to the filament stars. Evaluating the minimum of $F_{\text{II}}(B_i)$ for the filament-star data gives a magnetic field direction for the filament, B_{FIL} , toward $\ell = 359^\circ$, and $b = 19^\circ$. A better direction for the magnetic field direction traced by the filament stars is found in Frisch et al. (2015a, see Table 1), which incorporated new polarization measurements of three additional stars not used here. The polarization position angles expressed with respect to the pole B_{FIL} do not vary systematically with the distance of the star. Evidently the distance dependence of the polarization position angles defined by θ_{gal} is partly due to the rotation of the galactic coordinate system over the 90° span of the filament.

Figure 6, right, shows the polarization position angle that is calculated with respect to the filament magnetic field direction, B_{FIL} , and plotted against the angular distance between the star and the end of the filament. The filament end is defined by star HD 172167, located at $\ell, b = 67^\circ, 19^\circ$. The steady variation of the polarization angle $\text{PA}_{\text{filament}}$ along the filament length suggests that B_{FIL} provides a better coordinate system for expressing filament polarizations than does the north galactic pole (or north terrestrial pole). The best-fitting ISMF direction to the filament stars, from Equation (1), is directed toward the heliosphere nose defined by the inflow velocity vector of neutral interstellar He into the heliosphere. The magnetic turbulence associated with the filament polarizations is ± 9.6 , based on the harmonic mean of the measurement uncertainties and the dispersion of the polarization position angles with respect to the filament magnetic field direction. The polarization position angles of the filament are obviously not consistent with the local ISMF direction obtained in Paper II, or with the new fit to the entire data set in this paper (Figure 4, left).

Table 1
Interstellar Magnetic Field Directions

Magnetic Field	Merit ^a Function	ISMF Direction ^b ℓ, b (deg)
Paper I	Unweighted fit	38, 23 (± 35)
Paper II	$F_{\text{II}}(B_i)$	47 \pm 15, 25 \pm 20
All stars (B_{ALL})	$F_{\text{II}}(B_i)$	16.3, 27.0 (± 15)
Interstellar (B_{POL} , no filament stars)	$F_{\text{II}}(B_i)$	36.2, 49.0 (± 16)
Filament (B_{FIL} , only filament stars) ^c	$F_{\text{II}}(B_i)$	359.3, 19.0 (± 10.2)
<i>IBEX</i> (B_{IBEX}) ^d	...	34.8 \pm 4.3, 56.6 \pm 1.2
Angle between B_{POL} and $V_{\text{CLIC,LSR}}$ ^e	...	76.8 (+23.5, -27.6)
Angle between B_{POL} and B_{IBEX}	...	7.6 (+14.9, -7.6)
Angle between B_{IBEX} and $V_{\text{LIC,LSR}}$ ^f	...	96.9 \pm 8.5

Notes.

- ^a Equation (1).
- ^b The quantities ℓ, b are the direction of the ISMF in galactic coordinates.
- ^c Direction of the ISMF traced by the polarization filament, from Frisch et al. (2015a).
- ^d ISMF direction traced by the *IBEX* Ribbon, B_{IBEX} , corresponding to the weighted mean of the energy-dependent center of the *IBEX* Ribbon arc at $\lambda = 219.2 \pm 1.3, \beta = 39.9 \pm 2.3$ (Funsten et al. 2013).
- ^e Based on an upwind direction for the LSR CLIC velocity vector of $\ell = 335.6 \pm 13.4, b = -7.0 \pm 9.0, V = -17.3 \pm 4.9$ (Appendix D).
- ^f See Appendix D for the LSR velocity of the LIC.

4.3. Best-fitting Local Magnetic Field Direction without Filament Polarizations

Since the filament polarizations appear to define an isolated magnetic structure (see previous section), the fitting process has been repeated for a data set that is identical to that used to obtain B_{ALL} except that the thirteen stars that trace the filament polarizations are omitted. The results of the fit performed with the omission of the filament stars are shown in Figure 4, right,

Table 2
Polarization Data

Star	ℓ, b (deg)	Distance (pc)	θ_{RA}^a (deg)	Polarization ^b (10^{-5})	Source ^c
HIP 98130	9, -27	19	131.0 \pm 22.5	23.0 \pm 23.0	LNA
HIP 11276	354, -61	28	104.0 \pm 8.7	32.0 \pm 10.0	LNA
HIP 2790	316, -76	29	157.0 \pm 12.1	31.0 \pm 14.0	LNA
HIP 10301	279, -59	29	31.0 \pm 2.1	124.0 \pm 9.0	LNA
HIP 11197	14, -61	26	128.0 \pm 29.5	27.0 \pm 45.0	LNA
HIP 95467	329, -28	26	118.0 \pm 17.7	24.0 \pm 17.0	LNA
HIP 90355	37, 10	27	111.0 \pm 9.2	120.0 \pm 40.0	LNA
HD 105330	292, 31	33	95.0 \pm 25.9	45.0 \pm 57.0	LNA
HD 78351	258, 9	39	30.0 \pm 10.4	42.0 \pm 16.0	LNA
HD 111232	303, -5	30	92.0 \pm 32.4	30.0 \pm 64.0	LNA
HD 128674	317, 3	27	63.0 \pm 16.7	73.0 \pm 48.0	LNA
HD 177409	327, -27	35	133.0 \pm 15.4	37.0 \pm 22.0	LNA
HD 117939	312, 23	30	40.0 \pm 10.2	78.0 \pm 29.0	LNA
HD 125162	87, 64	30	25.0 \pm 15.0	2.72 \pm 1.45	KVA
HD 130109	355, 52	39	45.2 \pm 8.3	5.46 \pm 1.60	KVA
HD 132052	351, 46	28	45.7 \pm 31.6	1.88 \pm 2.32	KVA
HD 137391	60, 56	37	24.5 \pm 22.3	1.42 \pm 1.17	KVA
HD 175638	37, 0	40	85.0 \pm 27.3	2.10 \pm 2.16	KVA
HD 185395	82, 13	19	67.1 \pm 8.7	3.27 \pm 1.00	KVA
HD 19373	144, -7	11	25.2 \pm 8.7	4.04 \pm 1.24	KVA
HD 91889	258, 38	25	64.6 \pm 19.1	5.09 \pm 3.52	KVA
HD 124850	337, 51	21	148.5 \pm 23.0	1.38 \pm 1.17	KVA
HD 14055	142, -25	36	7.9 \pm 4.4	4.54 \pm 0.69	KVA
HD 15335	146, -28	31	21.4 \pm 14.9	4.28 \pm 2.28	KVA
HD 18256	160, -35	35	28.2 \pm 12.4	1.71 \pm 0.75	KVA
HD 18404	158, -33	32	27.0 \pm 14.1	1.03 \pm 0.52	KVA
HD 206901	78, -20	35	6.9 \pm 36.9	0.82 \pm 1.23	KVA
HD 222603	90, -56	31	21.7 \pm 37.3	1.17 \pm 1.78	KVA
HD 25490	184, -33	40	26.9 \pm 19.2	2.24 \pm 1.56	KVA
HD 25570	182, -31	36	24.5 \pm 10.9	2.59 \pm 1.00	KVA
HD 8829	155, -73	36	17.8 \pm 29.7	2.20 \pm 2.51	KVA
HD 13555	147, -37	30	11.3 \pm 13.8	2.45 \pm 1.20	KVA

Notes.

^a Polarization position angles are presented in equatorial coordinates.

^b The polarizations represent the fractional linear polarizations of the E -component of the starlight.

^c The data source refers to the telescope where the data were acquired. The KVA data were acquired by A. Berdyugin and V. Pirola using BVR filters. The LNA data were acquired by A. M. Magalhaes and D. B. Seriacopi using the V filter.

and the uncertainties on that fit are shown in Figure 5, right. For this new fit, the best-fitting ISMF direction is toward $\ell = 36^\circ.2$, $b = 49^\circ.0$. Comparison of the distribution of $F_{\text{II}}(B_i)$ for the evaluations with and without the filament stars (Figure 4), clearly shows that the merit function obtained from the star sample that omits the filament stars is more clearly defined than the irregularly shaped minimum of the merit function that is based on the entire data sample. The uncertainty on this best-fitting ISMF direction is assumed to occur where $F_{\text{II}}(B_i)$ is 10% larger than the minimum, giving an uncertainty on this direction of $\pm 16^\circ$ (Figure 5, right). The directions of B_{POL} and the *IBEX* ISMF, B_{IBEX} , are the same to within the uncertainties (Table 1).

4.4. Statistical Properties of the Merit Function for the Dominant ISMF, B_{POL}

At first glance, the excellent agreement between the ISMF direction obtained from the polarization data B_{POL} after stars tracing a separate magnetic structure are omitted from the sample and the ISMF traced by the *IBEX* Ribbon almost seems too good to be correct. Since other unrecognized magnetic features may be present in these data, and the volume of space

sampled by the polarization data is large, it is remarkable that the local ISMF field direction found from the polarization data is so close to the ISMF indicated by the *IBEX* Ribbon (Table 1). We therefore look more closely at the values of the individual parameters in Equation (1) to determine whether all of the polarization data with $P/\Delta P > 2.0$ are tracing B_{POL} , as opposed to B_{POL} being traced by only a subset of the polarization data.

The properties of the polarization position angles referenced to the best-fitting ISMF direction, B_{POL} , are viewed from two perspectives: (i) the three-dimensional statistical properties of $F_{\text{II}}(B_i)$ as a function of the probability G_n , $\text{sine}(\theta_{\text{POL}})$, and $F_{\text{II}}(B_i)$ evaluated for the polarization position angles calculated with respect to B_{POL} . (ii) The probability of the position angle (Equation (2)) versus the position angle of the star with respect to B_{POL} .

For the first approach, the statistical characteristics of the data set that yields the best-fitting ISMF can be represented by plotting the individual components of the merit function, $F_{\text{II}}(B_i)$ (Equation (1), Figure 7), where the best-fitting ISMF direction B_{POL} corresponds to the minimum value of $F_{\text{II}}(B_i)$. The function $f_n(B_i)$ (Equation (1)) achieves low values for

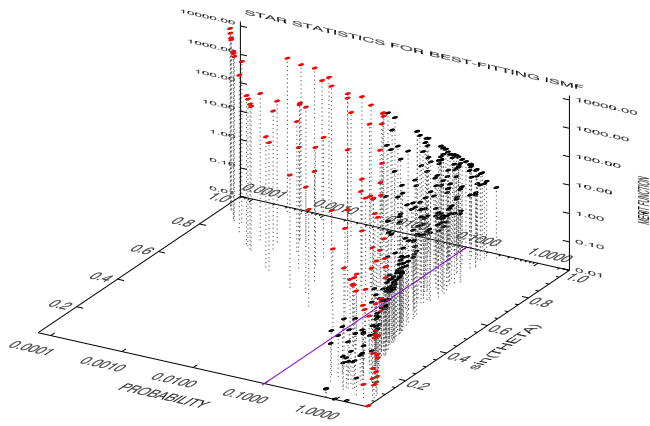


Figure 7. Distribution of merit function components in 3D. The value of the merit function $F_{II}(B_i)$ for each star determined with respect to B_{POL} , the best-fitting ISMF direction, is shown. The front horizontal axis shows the normalized probability, G_n , that the observed polarization position angle is equal to the expected angle for B_{POL} (Equation (2)). The right horizontal axis “sin(theta)” is the sine of θ_{PA} for each star in the coordinate system defined by B_{POL} located at the pole of the system. The vertical axis, “merit function” ($f_n(B_i)$) gives the merit function for each star (Equation (1)). Red points indicate stars with $P/\Delta P > 2.0$. This figure shows that the minimization method used to select out the best-fitting ISMF direction (Section 3) is sensitive to stars in the front-right hand corner of the figure, where the values of the merit function being minimized are small, and those in the rear left corner, where the measurement errors are small but the statistical probability that the value corresponds to the true angle represented by the best-fit is small. The stars in the rear left corner are candidates for tracing a new component of the local ISMF structure.

either high-probability polarization position angles (G_n , Equation (2)) or small $\sin(\theta_n)$. Figure 7 shows the $F_{II}(B_i)$ plotted against the probability G_n that the data point traces B_{POL} , and the sine of the position angle $\sin(\theta_{n,i})$ calculated with respect to the best-fitting ISMF $B_n = B_{POL}$. The probability shows the probability G_n (Equation (2)) for each star i , normalized to a maximum value of one. The right-hand axis labeled “sin(theta)” shows the sine of the polarization position angle for each star in the coordinate system defined with respect to the best-fitting ISMF at the north pole.¹⁵ The vertical axis labeled “merit function” shows the $f_n(B_i)$ for each individual star. Red points show stars where $P/\Delta P > 2.0$. The lower statistical probabilities of outlying polarization position angles for significant detections (e.g., $P/\Delta P > 2.0$) is apparent by the non-compliant position angles in the rear-left corner of the figure. Insignificant polarizations would not be expected in this corner since their position angles will tend to be statistically random so that $\sin(\theta_{n,i}) > 0$.

The distribution in Figure 7 can be used to identify the set of nearby stars with polarization position angles that are consistent with B_{POL} . These stars include stars where measurement uncertainties are either small, $P/\Delta P > 2.0$, or are large but with small values of $F_{II}(B_i)$ and $P/\Delta P \ll 2.0$. Appendix A lists the identifications of the top third of the stars with polarization position angles that provide the best match to B_{POL} and have $P/\Delta P > 2.0$. These stars are located on the front right of Figure 7. Stars with significant polarization position angles that do not comply with the direction of B_{POL} are in the rear left part of the figure, and represent

¹⁵ “North” refers to a geometric location and not the magnetic polarity in this context.

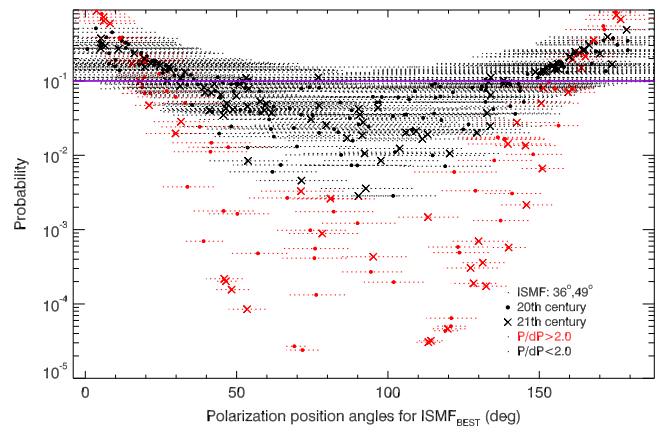


Figure 8. Statistical probabilities for individual stars. Statistical properties of the stars with respect to the best-fitting ISMF direction B_{POL} are plotted. The horizontal axis shows the polarization position angle in the rotated coordinate frame corresponding to the best-fitting ISMF direction B_{POL} (Table 1). The vertical axis gives the statistical probability (Equation (2)) of the data point. The red (black) points represent stars with polarization strengths of $P/\Delta P$ larger (smaller) than 2.0. Data collected during the 20th and 21st centuries are coded as “dots” and “crosses,” respectively. Polarization position angles that are perfectly aligned with B_{POL} have position angles of 0° or 180° . For reference, the purple line shows the same probability level as the purple line in Figure 7.

candidate polarizations for tracing an unrecognized component of the local ISMF (see Section 4.6).

Figure 7 shows that the minimization method used to select out the best-fitting ISMF direction (Section 3), will be affected both by the compliant stars in the front right-hand corner of the figure, where the values of the merit function being minimized are small, and by the non-compliant stars in the rear left corner where the probability that the observed polarization position angle corresponds to the true polarization angle (given by B_{POL}) is negligible. The general implication of Figure 7 is that a non-negligible fraction of the polarization position angles that are significant ($P/\Delta P > 2$) do not have polarization position angles that conform to (or are compliant with) the best-fitting ISMF. Those points are represented by low probabilities and large $\sin(\theta_{n,i})$ values in the figure. Stars with small values of $F_{II}(B_i)$ are referred to as stars that “conform” to, or are “compliant” with, the dominant ISMF direction B_{POL} .

Figure 8 shows the probability distribution of the stars as a function of the polarization position angle, θ_{POL} , evaluated with respect to the best-fitting ISMF, B_{POL} . Clearly stars with large measurement uncertainties are more likely to be compliant with the best-fitting ISMF B_{POL} than stars with small measurement uncertainties and polarization vectors pointing in the wrong direction. This feature allows data with all levels of accuracy to be useful in the fitting process. The second salient property of Figure 8 is that there are numerous polarization position angles that have small mean errors and also clearly do not trace the same magnetic field direction as B_{POL} and the *IBEX* Ribbon ISMF.

Figure 9 maps the stars in Figure 7 in the galactic coordinate system, and codes the symbol of the star as to whether or not the polarization position angle is compliant with B_{POL} . The star set is divided into two halves, based on the median value of $F_{II}(B_i)$ of 3.54. The best-matching half of the stars, where $F_{II}(B_i) < 3.54$, are plotted with solid symbols. The least-compliant half of the stars, $F_{II}(B_i) > 3.54$ are plotted with “X’s” (also see Figure 7). Stars where $P/\Delta P > 2.0$ are plotted

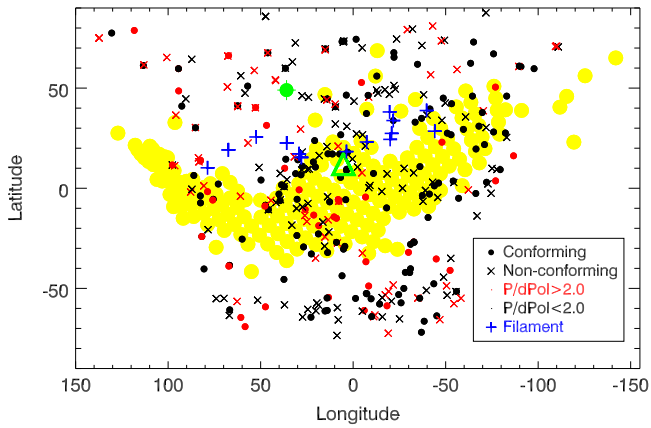


Figure 9. Stars used in the study are plotted with coding that indicates whether or not the polarization position angles agree with the ISMF field direction B_{POL} . The galactic locations of the stars in Figure 7 are plotted and coded by the value of $F_{\text{II}}(B_i)$ and $P/\Delta P$. The star set is divided into two equally sized groups, defined by stars that are in the top or bottom half of stars with polarization position angles that have polarization position angles that agree with the direction B_{POL} . Filled circles show the half of the data that best comply with B_{POL} , with stars having polarization mean errors of >2.0 plotted in red, and the less significant data points plotted in black. The stars with position angles that do not match θ_{POL} are plotted with “X’s.” The distribution of position angles that do or do not agree with B_{POL} are determined using the median value 3.54 of $F_{\text{II}}(B_i)$. The green triangle and green dot show the locations of the heliosphere nose, and the best-fitting ISMF B_{POL} , respectively. The blue crosses show the locations of the filament stars. Note that the stars which best trace the same ISMF as the *IBEX* ribbon tend to be more concentrated near the heliosphere nose and at lower galactic latitudes.

with red symbols, and stars with $P/\Delta P < 2.0$ are plotted with black symbols. The compliant stars with $P/\Delta P > 2.0$ have a tendency to be located between galactic longitudes of 0° and 90° in the northern hemisphere, and follow that trend until they wrap around ℓ at negative latitudes of $\sim -50^\circ$ in the southern galactic hemisphere near the BICEP2 region (Section 5.6). The conforming polarization position angles tend to follow into two extended distributions, one located roughly between ℓ , $b = 90^\circ$, 50° , and 60° , -60° , and the other extending roughly between 70° , 65° and -10° , -65° . There is a slight tendency for the southern hemisphere conforming polarization position angles to be located in the region of the original nearby dust “patch” identified by Tinbergen (1982) that extended to negative galactic latitudes in the fourth galactic quadrant ($\ell > 270^\circ$) of the galaxy.

4.5. Turbulence of Best-fitting ISMF B_{POL}

The turbulence in B_{POL} can be evaluated from the dispersion of the polarization position angles calculated with respect to the direction of the best-fitting ISMF direction B_{POL} . The third of the data sample that consists of the stars with ISMF directions that provide the best fit to B_{POL} contains 114 stars. Twenty-nine of those stars (listed in Appendix A) have significant polarizations with $P/\Delta P > 2.0$. A rough estimate of magnetic turbulence can be found by evaluating the polarization position angles in a coordinate system that is aligned with the pole of B_{POL} . The average position angle for this 29-star subset is $\theta_{\text{POL}} = 12^\circ 0 \pm 6^\circ 6$. This relatively small dispersion about the mean suggests that B_{POL} has a low level of magnetic turbulence, and is not twisted by the kinematical properties of the CLIC (Section 5.5).

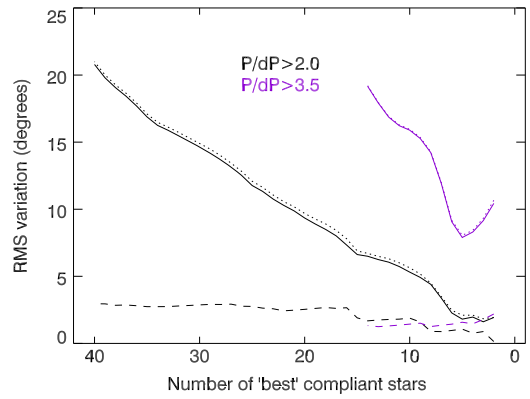


Figure 10. Component of the position angle dispersion that can be attributed to interstellar turbulence. The three quantities, interstellar turbulence, Φ_{IS} (solid lines), position angles θ_{POL} relative to the best-fitting ISMF direction B_{POL} (dotted lines), and mean measurement errors $\delta\theta_{\text{me}}$ (dashed lines) are displayed (see Equation (4)). Interstellar turbulence is evaluated both for the data subset consisting of 21st century measurements and $P/d\text{Pol} > 2.0$ (black), and $P/d\text{Pol} > 3.5$ (purple). The ordering of stars along the horizontal axis is according to the θ_{POL} , with the stars that best-agree with B_{POL} on the right of the horizontal axis, for the $P/\Delta P$ limits above. All positions on the lines represent results obtained by successively omitting the left-most (i.e. less compliant with B_{POL}) stars from the calculation of Φ_{IS} . The minimum for the $P/d\text{Pol} > 3.5$ data brackets the best approximation for the interstellar magnetic turbulence indicated by these data, $\Phi_{\text{IS}} \sim 9^\circ \pm 1^\circ$.

A better estimate of magnetic turbulence is obtained by considering only 21st century data that tend to have smaller mean errors than the older data. In the ideal case, the magnetic turbulence can be recovered by comparing the observed position angle variations with the mean measurement errors, or

$$\Phi_{\text{IS}}^2 = \text{std}(\theta_{\text{POL}})^2 - \text{std}(\delta\theta_{\text{me}})^2. \quad (4)$$

The quantity Φ_{IS} represents the calculated interstellar turbulence (in degrees), $\text{std}(\theta_{\text{POL}})$ is the standard deviation of the polarization position angle θ_{POL} evaluated for a coordinate system with the pole located at B_{POL} , and $\text{std}(\delta\theta_{\text{me}})$ is the standard deviation of the mean measurement errors of the data subset.

The amount of interstellar turbulence obtained from Equation (4) varies with the number of stars that are included in the data subsample. If this subgroup of high-quality polarization data is sorted numerically according to goodness-of-fit between θ_{POL} and B_{POL} , where the perfect measurement will have $\theta_{\text{POL}} = 0^\circ$, then the end-point of the array that contains the stars with the very best matches between the polarization position angles and B_{POL} should also provide the best estimate of the interstellar magnetic turbulence using Equation (4). In Figure 10 we evaluate interstellar turbulence using Equation (4) and by starting with the highest quality data set established by setting some minimum value for $P/\Delta P$. That data subset is then reevaluated by successively rejecting the lowest quality data points until a reasonable estimate for the interstellar turbulence is obtained. Figure 10 shows the estimates of interstellar turbulence (solid lines) for two data subsets with $P/\Delta P > 2.0$ (black lines) and $P/\Delta P > 3.5$ (purple lines). The horizontal axis shows the number of qualifying stars included in the numbers used in Equation (4), with the stars with polarization position angles that better match B_{POL} on the figure right, and those with poorer matches on the figure left. For a data subset that is restricted to stars with $P/\Delta P > 3.5$, the minimum value of the interstellar turbulence

is 8° and the seven stars that bracket this minimum have $\Phi_{\text{IS}} = 9^\circ \pm 1^\circ$.

For a larger subset where $P/\Delta P > 2.0$, the minimum of the interstellar turbulence decreases to $\sim 2^\circ$ for the stars that best-comply with B_{POL} . However, the turbulent component of the ISMF B_{POL} should be best defined by the most precise data, so we report the turbulence $\Phi_{\text{IS}} = 9^\circ \pm 1^\circ$ from the $P/\Delta P > 3.5$ data subset as the our best estimate of the turbulence of B_{POL} .

4.6. Polarization Data not Assigned to an ISMF Structure

The large number of non-conforming stars in Figure 9 suggests that one or more additional ISMF directions, not yet accounted for, must be influencing some of the polarization position angles. B_{POL} is based on 360 measurements, of which 33% have $P/\Delta P > 2.0$. The set of stars with the largest third of the values of the $F_{\text{II}}(B_i)$ (i.e., the one-third of the polarization data that are least compliant with the direction B_{POL}) were selected to be tested independently for a direction of the ISMF using the method described in Section 3. The best-fitting ISMF direction for this third of the stars is toward $\ell = 267^\circ.3$, $b = 33^\circ.0$, which is 86° from the heliosphere nose and is marginally constrained since it is at the edge of the region that is included in this study.

5. DISCUSSION

5.1. Comparing the Magnetic Field Directions Obtained from the Polarization Data and the IBEX ENA Ribbon

IBEX measures ENAs created from charge-exchange between neutral interstellar atoms and heliosheath ions, including the solar wind and incorporated pickup ions (McComas et al. 2009; Livadiotis & McComas 2012). IBEX discovered an extraordinarily circular Ribbon of ENAs that is about 20° wide and several times more intense than the distributed flux of ENA emissions throughout the rest of the sky (Fuselier et al. 2009; McComas et al. 2009; Schwadron et al. 2011; Funsten et al. 2013). The locus of sightlines where the Ribbon is observed appear in directions where the ISMF draping over the heliosphere is perpendicular to the radial viewing sightline (Schwadron et al. 2009). There is no consensus agreement on the Ribbon formation mechanism (McComas et al. 2014). More recently, Schwadron & McComas (2013) and Isenberg (2014) have suggested that the Ribbon is created through retention of pickup ions, implying that the Ribbon reflects a true spatial structure, not an optical effect due to the prominence of the pickup ring, as previously discussed (McComas et al. 2009; Heerikhuisen et al. 2010). The Ribbon geometry is a sensitive diagnostic of the ISMF direction and strength, and the pressure and ionization of the interstellar cloud surrounding the heliosphere (Frisch et al. 2010b; Heerikhuisen & Pogorelov 2011; Ratkiewicz et al. 2012).

The IBEX Ribbon is a highly circular feature, with a radius of $74^\circ.5 \pm 2^\circ.0$ that is centered on the ecliptic coordinates of $\lambda = 219^\circ.2 \pm 1^\circ.3$, $\beta = 39^\circ.9 \pm 2^\circ.3$ (based on the weighted mean average over the energy passbands, Funsten et al. 2013). The Ribbon center corresponds to galactic coordinates of $\ell = 34^\circ.7 \pm 4^\circ.3$, $b = 56^\circ.6 \pm 1^\circ.2$. The Ribbon center is energy dependent and shifts by $9^\circ.2$ across the five energy bands of IBEX-HI, from $\ell = 34^\circ.7$, $b = 55^\circ.5$ for the 0.7–1.7 keV bands, to $\ell = 20^\circ.1$, $b = 60^\circ.7$ for the 4.3 keV band, in galactic coordinates.

The observed center of the Ribbon arc is likely to be within 5° of the true ISMF direction outside of the heliosphere. MHD simulations of the Ribbon formation by Heerikhuisen et al. (2014) show that the center of the Ribbon arc is offset from the direction of the ISMF far upstream of the heliosphere by 5° for interstellar field strengths of $3 \mu\text{G}$. Comparisons between the pressures of the inner heliosheath plasma and the thermal and ram pressure of the LIC give an ISMF of $\sim 3.3 \mu\text{G}$. A similar value of $\sim 3.1 \mu\text{G}$ is found from the magnetic distortion of the heliotail (Schwadron et al. 2011). Photoionization models of the LIC that include energy sinks and sources also predict a $\sim 2.7 \mu\text{G}$ magnetic field strength from the equipartition of energy (Slavin & Frisch 2008).

The direction of the best-fitting ISMF that is obtained from the data set that omits the filament stars, B_{POL} , agrees remarkably well with the magnetic field direction that is obtained from the center of the IBEX Ribbon arc. The angular separation between the magnetic field direction that dominates the results obtained from the polarization data, B_{POL} , and the IBEX Ribbon field direction is $7^\circ.6 (+14^\circ.9, -7^\circ.6)$ (Table 1). The uncertainties become larger if the energy variation of the Ribbon center is included. The alignment of B_{POL} and B_{IBEX} indicate that these two magnetic field directions are the same to within the uncertainties, and that the ISMF interacting with the heliosphere extends into the upwind interstellar regions with minimal distortion outside of the draping region. It is also possible that B_{POL} agrees with B_{IBEX} because B_{IBEX} is the nearest coherent magnetic structure in the sky and therefore has the largest angular extent of all possible ordered fields.

Stars with polarization position angles that differ from B_{POL} , and therefore from B_{IBEX} , have slightly stronger polarization strengths than those that do not agree. However, there does not appear to be any difference between the distances of the two subsets of the data. The third of the polarization data that provides the worst match to B_{POL} consists of 114 measurements that have a mean $P/\Delta P$ of 2.4 ± 1.5 . The third of the polarization set that provides the best match to B_{POL} has a mean $P/\Delta P$ of 1.5 ± 1.1 . Both sets of stars have mean distances of approximately 25 ± 10 pc. The lower mean significance of the polarizations that provide the best match to B_{POL} , and therefore B_{IBEX} , is not surprising since total dust column densities will be lowest for the ISM closest to the heliosphere.

The polarity of the ISMF is not given by either the IBEX Ribbon data or by the polarization data. Both the polarity of the ISMF direction found by Voyager 1 at the heliopause (Burlaga & Ness 2014), and the radio rotation measures of pulsars within several hundred parsecs in the fourth galactic quadrant (Salvati 2010), suggest a polarity for the local ISMF that is directed upwards through the galactic plane.

5.2. Galactic Cosmic Ray Asymmetries

Asymmetries in the flux of TeV galactic cosmic rays at Earth are observed over both large (Nagashima et al. 1998; Abdo et al. 2009) and small (Veronetto et al. 2009; Abbasi et al. 2011; Tibet As γ Collaboration et al. 2011) angular scales. The cosmic rays in the 1.5–10 TeV energy range have gyroradii of ~ 100 – 700 AU in a $3 \mu\text{G}$ magnetic field, and probe the magnetic field in the same spatial region as the IBEX Ribbon (Schwadron et al. 2014). Schwadron et al. modeled galactic cosmic ray streaming along the ISMF, for a small ratio of the perpendicular-to-parallel component of diffusion, and showed

that the observed TeV cosmic ray asymmetries show a general ordering about the equator of B_{IBEX} locally. Over larger spatial scales, interstellar magnetic turbulence may disrupt GCR streaming and reduce the magnitude of the GCR asymmetries.

The low level of magnetic turbulence found for B_{POL} , $\Phi_{\text{IS}} \sim 9^\circ \pm 1^\circ$, indicates that the *IBEX* magnetic field extends out into interstellar space where the low magnetic turbulence does not impede the flux of TeV GCRs into the heliosphere. Over spatial scales of several hundred parsecs, Salvati (2010) used the rotation measures of radio sources to determine a direction for the ISMF in the third galactic quadrant that is within $\sim 22^\circ$ – 24° of B_{IBEX} . Both the polarization data and the radio rotation measure data suggest that the *IBEX* Ribbon traces a non-turbulent magnetic field that extends into the third galactic quadrant from whence the GCR streaming arrives.

5.3. Possible Origins of the Magnetic Filament

The origin of the filamentary structure (or structures) defined by the polarization position angles plotted in Figure 6 is not firmly established. The filament polarizations trace an ISMF direction that is aligned with the direction of the heliosphere nose, and the filament stars are spatially arranged along a direction that is perpendicular to the $B_{\text{ismf, helio}} - V_{\text{vel, helio}}$ plane that marks the heliosphere asymmetry created by the ISMF at the heliosphere, $B_{\text{ismf, helio}}$ and the heliocentric interstellar gas velocity at the heliosphere, $V_{\text{vel, helio}}$. These properties led to the proposal that the filament polarizations are evidence for the deflection of the polarizing interstellar dust grains around the heliosphere (Frisch et al. 2015a). Confirmation of a filament origin in the outer heliosheath will require modeling the alignment and transport of interstellar dust grains during their approach to, and interaction with, the heliosphere. As this modeling is not yet available, other possible origins for the filament are briefly mentioned.

An alternate origin for the filament polarizing grains could be that the grains are near the Sun and embedded in the LIC flow, but outside the influence of the heliosphere. Since the ISMF that is the best fit to the filament polarizations coincides with the heliosphere nose direction, which is defined by the inflowing interstellar He° , this interpretation requires that either the ISMF traced by the filament is parallel to the heliocentric LIC gas velocity, or that the assumption of polarization vectors parallel to the magnetic field direction is invalid. The first requirement invokes a random coincidence between the filament ISMF direction and the LIC heliocentric velocity and violates the result that the LIC magnetic field and LSR velocity are perpendicular based on *IBEX* data (Table 1, Schwadron et al. 2015a). The second requirement may be fulfilled if radiative alignment is significant (e.g., Hoang & Lazarian 2014; Andersson 2015).

Alternatively, if B_{FIL} is not associated with the LIC but is located at a distance of ~ 5 pc from the Sun, then the filament extent is about 1.7×7.1 pc in the plane of the sky. If this feature has the same density as the LIC ($n \sim 0.26$ H° nuclei cm^{-3} , Model 26 in Slavin & Frisch 2008), then the column density associated with the feature would be $\log N(\text{H}^\circ) = 18.14$ cm^{-2} . Such a column density would be consistent with other column densities through the very local ISM (Wood et al. 2005). However, the coincidence between the

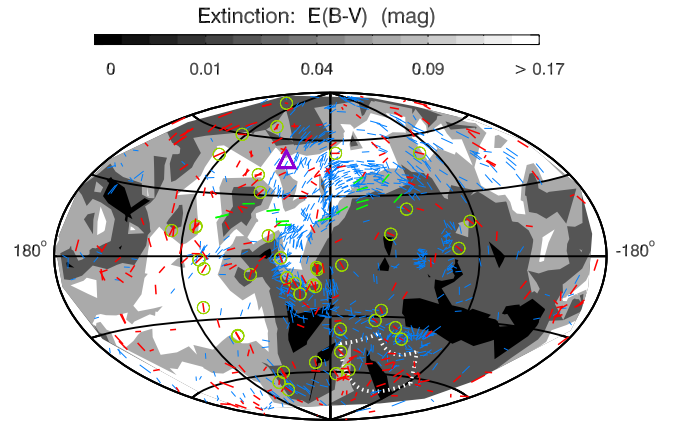


Figure 11. Amount of reddening of nearby stars is compared to polarized starlight. Reddening is represented by the cumulative smoothed color excess $E(B - V)$ of stars within 100 pc (Appendix B). The polarizations of stars within 40 pc are plotted with red bars, except that the filament polarizations are plotted with green bars. Nearby stars with polarization position angles that are in the best agreement with B_{POL} have green circles around them (see text). The polarizations of stars within 300 pc and that define Loop I are plotted with blue bars. The polarization patterns for the distant and nearby stars are similar in many regions suggesting that they are sampling a common magnetic field direction that is ordered by Loop I. The dominant nearby dust structure (lightest coloring) surrounds a cavity of low extinction centered below the galactic plane in the fourth galactic quadrant (central dark region). Loop I models suggest the dust structure is from the expansion of Loop I into the Local Bubble. The polarizations of southern hemisphere stars are more likely to trace B_{POL} than northern hemisphere stars. The ISMF in the region tested by BICEP2 for the B-mode polarizations of the CMB (dotted lines) is different from B_{POL} . The direction of B_{POL} is shown by the purple triangle.

filament ISMF direction and the heliosphere nose would remain puzzling.

The filament could be associated with an unidentified magnetic field component, perhaps associated with a shock front related to Loop I that extends very close to the Sun. For this possibility, again, it is a coincidence that the best-fitting ISMF to the filament polarizations is toward the heliosphere nose. The shock could be associated with the ISM in front of one of the filament stars, α Oph (HD 159561, A5 III, 14 pc), where high abundances of refractory elements in the gas, a strong Mg° line indicating high temperature or electron densities, and temperatures up to 23,000–60,000 K indicate the processing of dust through interstellar shocks (Frisch 1981; Frisch et al. 1987, 1999; Crawford 2001). The polarizations of the star HD 159561 that traces the filament was measured at high sensitivity by both PlanetPol (Bailey et al. 2010) and POLISH2 (Wiktorowicz et al. 2015), with good agreement between the polarization position angles.

Figure 11 compares polarization directions with the configuration of dust reddening that is associated with the parts of Loop I within ~ 100 pc (Appendix B contains additional information about the figure). Some of the filament stars have polarizations that are loosely parallel to the edge of the cavity in the distribution of the dust extinction. The sample of polarized stars within 40 pc has been divided into two parts, and the half with polarization position angles in best agreement with the very local ISMF B_{FIL} are circled. The filament polarizations for stars between $\ell = 20^\circ$ and $\ell = 90^\circ$ are not aligned with strong gradients in the cumulative color excess in Figure 11, so a possible association between the filament and Loop I requires further study.

5.4. Polarization Efficiency in Local ISM

Measurements of starlight that has been polarized in the ISM provide one of the few viable methods for determining the distribution of nearby interstellar dust grains and understanding the relative distributions of interstellar gas and dust over parsec-sized scale lengths. Polarization efficiencies in the local ISM can be found by comparing polarization strengths with color excess $E(B - V)$, and $E(B - V)$ with hydrogen column densities. Column densities of H^0 for stars within 40 pc are typically less than $N(H^0 + 2H_2) \leq 10^{18.7}$ (Wood et al. 2005). Using the mean ratio between $N(H^0) + 2NH_2$ and $E(B - V)$ (Bohlin et al. 1978), and the upper envelope of the relation between polarization and $E(B - V)$ (Serkowski et al. 1975) yields $E(B - V) \leq 0.0009$ mag and $P_{\%} \leq 0.008$ for the very local ISM. Using instead the analogous relations that apply to low-extinction stars with low column densities of foreground H_2 predicts $E(B - V) \leq 0.001$ mag and $P_{\%} \leq 0.014$ in the local ISM. A quantitative discussion of the relations in this subsection that link hydrogen column density and polarization strength is given in Appendix C.

It might be expected that interstellar polarizations of nearby stars will be more effective than the polarizations of distant stars since the ISM toward distant sources is likely to be more complex, with different magnetic field directions or strong radiation fields in the sightline depolarizing a polarized beam. Variations in alignment efficiency are also indicated by theoretical calculations of perfectly aligned infinite cylinders that show approximately a factor 3–4 larger $P_{\%}/E(B - V)$ than is observed (Mathis 1979; Kim & Martin 1994). The efficiency of nearby interstellar polarization can be tested using stars where both polarization data and hydrogen column density are available. Two variables are introduced to trace the efficiency of the polarization in a sightline, α and α' . The ratio $P_{\%}/E(B - V)$ is proportional to α and α' for high-column density and low column density sightlines, respectively. Since $N(H^0)$ will be used as a proxy for $E(B - V)$ for the nearby stars (Appendix C) a third variable $\gamma = N(H^+)/N(H^0)$ is included to account for the possible presence of ionized hydrogen.

Both polarization and UV absorption line data are available for the nearby star HD 34029 (α Aur, Capella, 13 pc Wood et al. 2002). Combining UV and FUV data on Capella, and adopting a model for the cloud length, Wood et al. determined column densities of $\log N(H^0) = 18.24 \pm 0.07$ cm⁻² and $\log N(H^+) = 18.08 \pm 0.65$ for the LIC in this direction, corresponding to $\gamma \sim 0.69$ (with large uncertainties, ± 1.47). The polarization of Capella is $P(\%) = 0.024 \pm 0.009$ (Piirola 1977). Combining these values with Equations (8) and (12) in Appendix C for reddened and unreddened sightlines respectively gives $\alpha \sim 5.3$ and $\alpha' \sim 2.6$, where both estimates have large uncertainties. These large values for polarization efficiency compared to the expected values of one for the upper envelope of the relation between polarization and color excess of distant stars (Appendix C) suggest that polarization mechanisms in the local ISM are more efficient than for distant reddened and low-extinction stars. These results are nevertheless highly uncertain both because measurement uncertainties are large and Capella is a G1III+K0III binary system where intrinsic polarization is possible.

A second test of alignment efficiency in the local ISM is made using the two stars with spectral types not associated with intrinsic polarization, HD 11443 (F6IV, 20 pc) and 39587 (G0V, 9 pc) that have polarizations of $P_{\%} = 0.02 \pm 0.009$ and

0.019 ± 0.008 respectively (Piirola 1977). For these stars $\log N(H^0) = 18.33$ cm⁻² and $\log N(H^+) = 17.93$ cm⁻², respectively (Wood et al. 2005). Information on H^+ toward these stars is not available so the Capella value for γ is assumed. The resulting alignment efficiencies are $\alpha = 3.6$, and $\alpha' = 1.9$ for HD 11443, and $\alpha = 8.5$ and $\alpha' = 3.7$ for HD 39587. If lower ionization levels had been assumed, such as $\gamma \sim 0.29$ corresponding to the fractional ionization of the LIC near the heliosphere (Model 26 in Slavin & Frisch 2008), these values of α and α' would increase.

These estimates of the polarization efficiency in the local ISM, where $\alpha > 1$, are consistent with the results of Fosalba et al. (2002) who found a nonlinear increase in polarization as extinction approached zero for low column density stars (see Appendix C). The low column density values of $\alpha' > 1$ found in the previous paragraph could be spurious, resulting from the combination of the large uncertainties and this nonlinear behavior of polarization strengths at low column densities. Further data on both interstellar column densities and polarizations toward the same stars are needed to establish the efficiency of the polarization mechanisms in the local ISM.

5.5. Nearby Magnetic Field, Loop I Superbubble, and the Local Interstellar Cloud

The agreement between B_{IBEX} and B_{POL} (Table 1) indicates that B_{IBEX} extends into the ISM without significant distortion. The low level of magnetic turbulence for B_{POL} (Section 4.5) suggests that the ratio of the plasma thermal to magnetic pressure, β , is ≤ 1 . A LIC magnetic field strength of ~ 3 μ G is consistent with the total interstellar pressure required to balance the inner heliosheath plasma traced by *IBEX* ENAs, and the deflection of the heliotail to the port side¹⁶ of the heliosphere (Schwadron et al. 2011), and also the equipartition of energy between the LIC thermal gas and magnetic field (Slavin & Frisch 2008). Nearby polarized stars with significant polarizations that do not trace B_{POL} (Section 4.6) may indicate local regions where the magnetic field has been distorted by cloud motions that create high magnetic pressure (Figure 13), or by cloud collisions (Figure 12).

The local magnetic field, B_{POL} , provides a probe of the physical properties and origin of the interstellar cloudy material in the immediate solar neighborhood. The bulk motion through space of the nearby interstellar material associated with the CLIC, < 30 pc, has been determined from the velocities for interstellar optical and UV absorption lines and the flow of interstellar dust through the heliosphere (Frisch et al. 2011). The angle between B_{POL} and the upwind direction of the CLIC LSR velocity ($V_{CLIC,LSR}$, Appendix D) is $76^{\circ}8 (+23^{\circ}5, -27^{\circ}6)$. Although the uncertainties are large, the bulk motion of local interstellar gas relative to the LSR is therefore perpendicular to the ISMF direction. The flow of the CLIC relative to the LSR originates in a direction that is within $21^{\circ}4 \pm 20^{\circ}8$ of the nominal center of the Loop I superbubble. For the Loop I bubble center, we use the S1 shell feature, centered at $\ell = 346^{\circ} \pm 5^{\circ}$, $b = 3^{\circ} \pm 5^{\circ}$ as defined by (Wolleben 2007). The S1 bubble model places the Sun in the

¹⁶ The nautical terms “starboard” and “port” have been adopted to describe the flanks of the heliosphere to the right and left, respectively, of the heliosphere nose when referenced to the ecliptic coordinate system. In galactic coordinates this therefore places the starboard side of the heliosphere *mostly* in the fourth galactic quadrant at positive latitudes, and the port side of the heliosphere in the fourth galactic quadrant and *mostly* at negative latitudes.

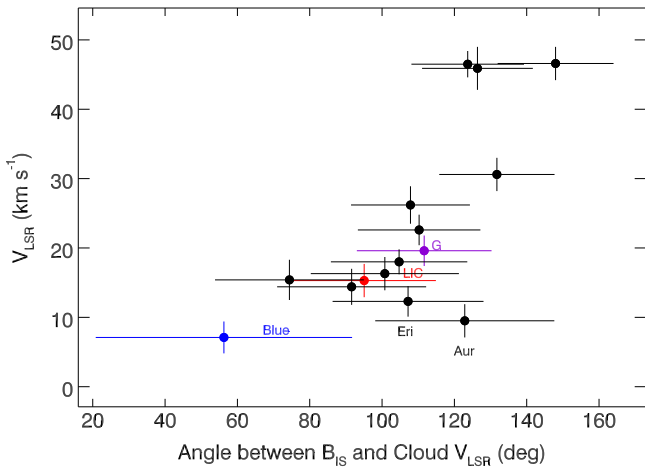


Figure 12. LSR velocities of the 15-cloud model for the CLIC (see the text) are plotted against the angle between the LSR velocity and the magnetic field direction B_{POL} . The LSR velocity increases with the angle between V_{LSR} and B_{POL} , except for the labeled Eri and Aur clouds. Over half of the clouds travel at an angle that is quasi-perpendicular to B_{POL} at angles 90° – 120° .

rim of the S1 shell. The relative configurations of B_{POL} , V_{CLIC} , V_{LSR} , and the S1 bubble form a self-consistent picture where local ISM, consisting of the CLIC, is part of the rim of the Loop I superbubble and B_{POL} represents the magnetic field swept up in the rim of the expanding superbubble.

The *IBEX* measurements of the LIC velocity and LIC magnetic field provide a precise set of data for comparisons between the LIC interstellar gas velocity and magnetic field vectors. The heliocentric velocity determined by *IBEX* for interstellar He° flowing through the heliosphere corresponds to a LIC velocity with respect to the LSR of $V_{\text{IBEX, LSR}} = 17.2 \pm 1.9 \text{ km s}^{-1}$ toward $\ell, b = 141.1 \pm 5.9, 2.4 \pm 4.2$ (based on the velocity in Schwadron et al. 2015b). The direction of the ISMF that shapes the heliosphere is given by the weighted mean center of the *IBEX* Ribbon, at $\ell = 34.8 \pm 4.3, b = 56.6 \pm 1.2$ (Table 1, Funsten et al. 2013). The perpendicular angle between the LIC velocity with respect to the LSR, and the *IBEX* magnetic field direction (96.9 ± 8.5 , also see Schwadron et al. 2014) indicates that the motion of the LIC through space is consistent with a scenario where the partially ionized LIC sweeps up and carries a frozen-in magnetic field through space (Model 26 in Slavin & Frisch 2008, indicates that $\sim 22\%$ of the hydrogen and $\sim 39\%$ of the helium are ionized).

Different aspects of this picture emerge when the 15-cloud model of Redfield & Linsky (2008) is compared with the direction of the interstellar field. The angles between the LSR velocities of the fifteen clouds (given in Frisch & Schwadron 2014) and B_{IBEX} are plotted in Figure 12 against V_{LSR} . The magnetic field direction is represented by the *IBEX* value, as B_{IBEX} is known more precisely than the field determined from the polarization data, B_{POL} , and the two field directions agree (Table 1). A prominent characteristic of Figure 12 is that, except for the Aur cloud, the LSR velocities of these clouds tend to increase as the angle between V_{LSR} and the interstellar field increases if the uncertainties are included. The mean angle between the 15 LSR velocities and B_{IBEX} is 107.5° .

If we assume that deviations of the velocities of the 15 individual clouds from the bulk CLIC motion are caused by the

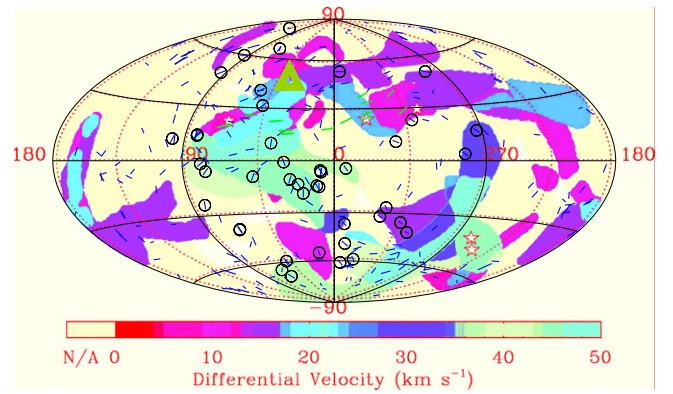


Figure 13. Polarizations of stars with mean errors $> 2\sigma$ are plotted on a representation of the differential velocities between clouds in the same sightline. The underlying velocity differential figure is a recolored version of Figure 2 in Linsky et al. (2008). High differential velocities suggest colliding clouds. The polarizations of stars that conform to B_{POL} are circled. The polarization vectors are shown for stars with $P/\Delta P > 2.0$, and color coded with non-filament/filament polarizations in blue/green. Circled stars correspond to compliant stars in Figure 11. B_{POL} is found in the directions of clouds with velocities that span the entire range of differential velocity space from 0 to 50 km s^{-1} , but favors locations in the first galactic quadrant.

injection of energy into the CLIC gas, and that the energy injection is ordered by the pole of the *IBEX* ISMF direction B_{POL} (Table 1), then the most effective acceleration is directed toward the antipode of B_{POL} at $\ell = 216^\circ, b = -49^\circ$. The largest deviations from the perpendicularity of the gas and magnetic field therefore occurs for higher velocities that are more pointed toward the third galactic quadrant, where gas and dust densities are extremely low (e.g., Fitzgerald 1968; Frisch & York 1983; Vergely et al. 2010).

The CLIC is a decelerating flow of interstellar gas so that cloud collisions supply an opportunity for shock formation (Frisch et al. 2002; Linsky et al. 2008; Redfield & Linsky 2008; Gry & Jenkins 2014; Frisch et al. 2015c). Stars that are compliant with B_{POL} are preferentially located in the first galactic quadrant, $\ell = 0^\circ$ – 90° (Figure 13). Some of the stars that have polarizations that are compliant with B_{POL} (Section 4.4, and are circled in Figure 9) are also located in kinematically active regions. The elongated feature of compliant stars with $\ell = 60^\circ$ – 90° (Section 4.4) occupies a kinematically quiescent region (Figure 13) dominated by the LIC, while the second elongated feature with $\ell = -10^\circ$ – 70° occurs in a kinematically active region where multiple clouds and large differences in absorption component velocities in the same sightline indicate cloud collisions at up to 50 km s^{-1} .

It is notable that there is minimal nearby polarization associated with the G-cloud centered near $\ell, b = 315^\circ, 0^\circ$ (Figures 13, 14). Two stars with polarization position angles that comply with B_{POL} are found toward the G-cloud (Figure 13). Two layers of nearby polarizing dust are found in the direction of the G-cloud, at ~ 19 and ~ 55 – 65 pc (Figure 14). The G-cloud extends in front of α Cen, at 1.3 pc, but the polarizing grains are much more distant.

The G-cloud region shows evidence of dust grain destruction by interstellar shocks. The average volume densities of interstellar Fe and Ca are systematically larger in the third and fourth galactic quadrants where the G-cloud is located, compared to $\ell < 180^\circ$ (Frisch 2010). Destruction of dust grains in interstellar shocks preferentially returns refractory elements such as Fe and Ca to the gas phase (Jones et al. 1994; Frisch

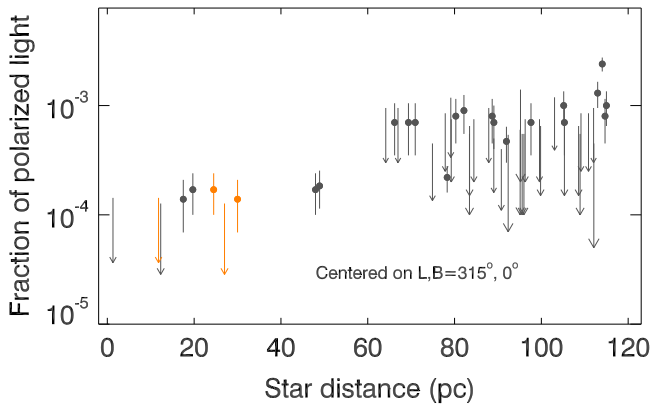


Figure 14. Polarizations are plotted for stars within 20° of the nominal center of the G-cloud at $\ell, b = 315^\circ, 0^\circ$ (according to the model of Redfield & Linsky 2008). Two layers of polarizing grains are seen, at ~ 19 and ~ 60 pc. The arrows show upper limits on polarizations $P/\Delta P < 2.0$.

et al. 1999), so that the higher Fe and Ca densities in the G-cloud region may indicate recent shock activity and magnetic turbulence.

5.6. Starlight Polarizations in the BICEP2 Field

Interstellar polarization data provide one technique for selecting the dust-free sightlines that provide the optimum conditions for measurements of the B-mode polarization of the cosmic microwave background (CMB). BICEP2 has studied the B-mode polarization in a southern region centered near R.A. = 0° , decl. = -57.5° (Ade & the BICEP2 team 2014). The BICEP2 field coincides roughly to the region defined by decl. between -68° and -48° , and R.A. between 322° and 38° . This field, centered on galactic coordinates $\ell, b = 316^\circ.1, -58^\circ.3$, is outlined with dotted lines on a smoothed map of color excess $E(B - V)$ for stars within 100 pc in Figure 11 (also see Figure 3). Figure 15 shows that the BICEP2 region contains significant polarization within 40 pc of the Sun, and with increasing polarization strengths out to 300 pc. The star that is circled at the high-longitude end of the BICEP2 region (Figure 11) indicates a star with a polarization position angle that conforms to B_{POL} , and therefore to B_{IBEX} , which suggests that B_{IBEX} extends up to the edge of the BICEP2 region. A slightly different ISMF direction is traced by most of polarized stars in the BICEP2 region.

We have tested the dust content of the BICEP2 field using two markers of interstellar dust, optically polarized starlight and the color excess $E(B - V)$ of stars. The polarization data for stars in this field are plotted against distance in Figure 15, using the data sources mentioned in Section 2. Both significant polarization detections where $P/\Delta P \geq 2.0$, and lower polarization strengths that are not statistically significant are found. Polarizations are up to $\sim 0.2\%$, corresponding to color excess values of $E(B - V) \geq 0.028$ mag (using the low extinction relations of Equation (9) for $\alpha' \leq 1$), optical extinction $A_V = 3.1 * E(B - V) \geq 0.087$ mag for an assumed selective-to-total extinction of 3.1, and column densities of $N(\text{H}) \geq 1.4 \times 10^{20} \text{ cm}^{-2}$. The starlight reddening data that give the color excess values in Figure 11 (see Appendix B) indicate larger color excesses of $E(B - V) > 0.2$ mag through the BICEP2 field, or optical extinctions of $A_V > 0.6$ mag for a selective-to-total extinction ratio of 3.1.

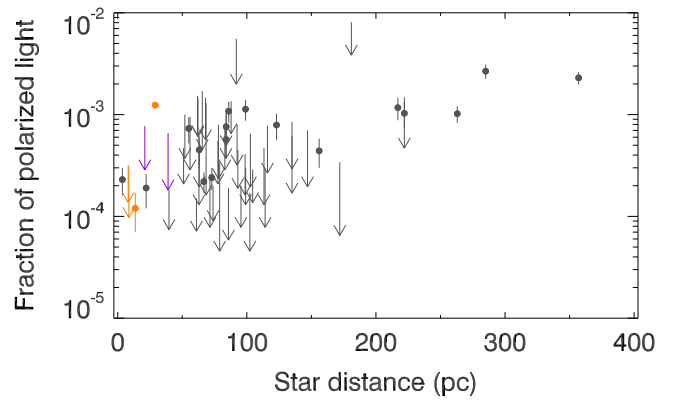


Figure 15. Polarizations of stars located in the BICEP2 field are plotted against distance. The observed polarizations suggest that the opacity in the $B - V$ band in this field is $A_V \sim 0.069$ mag or more, depending on foreground depolarization. The two nearby stars with detected polarizations in the BICEP2 field and observed by LNA are HD 211415 and HIP 10301 (see symbol color-coding of Figure 3).

Although the extinction of the BICEP2 region is negligible when compared to molecular clouds, the polarization data show that the dust that is present produces detectable amounts of optical polarization in the starlight. Both B_{POL} and the lower latitudes of Loop I extend into the BICEP2 region where they indicate that the local contributions to polarizations are likely to trace an ordered magnetic field with directions that can be predicted from the measurements of the very local ISMF B_{POL} and the southerly portion of Loop I.

6. CONCLUSIONS

Starlight that is linearly polarized while traversing the dichroic local ISM is utilized to chart the direction of the magnetic field within 40 pc and 90° of the nose of the heliosphere, corresponding roughly to the galactic center hemisphere. The purpose of the study is to compare the direction of the ISMF that shapes the heliosphere, and is traced by the unconventional magnetic field diagnostic provided by the *IBEX* ENA Ribbon, with the local ISMF direction traced by the polarization data.

New data on polarized starlight acquired in the northern and southern hemispheres provide the basis for this study. These polarization measurements, with typical 3σ sensitivities of 0.01%, have been collected with telescopes at the KVA, LNA, and Lick observatories. Using the new polarization data and additional data from Paper II and the literature, we determine several nearby magnetic structures, one of which coincides in direction with the ISMF traced by the *IBEX* Ribbon. Summarizing the results:

1. A merit function, $F_{\text{II}}(B_i)$, has been developed for evaluating the magnetic field direction that best fits the polarization data. $F_{\text{II}}(B_i)$ assumes that the linear interstellar polarizations are parallel to the magnetic field direction. Evaluation of the merit function for the entire qualifying set of polarization data, within 40 pc and 90° of the heliosphere nose direction, results in a local ISMF direction in agreement with earlier values in Paper II.
2. A visually and numerically distinct magnetic filament is traced by the polarizations of thirteen stars, of which the nearest star is within six parsecs. These filament stars were originally selected based on a gradient of the polarization

position angles with distance, for position angles given in the galactic coordinate system, but that effect was found to be spurious (Section 4.2). Utilizing the function $F_{II}(B_i)$ to obtain the ISMF direction that is traced by the filament polarizations gives an ISMF direction that is located within $15^\circ \pm 10.3$ of the heliosphere nose. Frisch et al. (2015a) favor an origin for the filament polarizations related to the interstellar dust that is deflected around the heliosphere in the outer heliosheath. Other possibilities are that the feature is associated with the local ISM or possibly related to the near side of Loop I.

3. The ISMF that shapes the heliosphere, B_{IBEX} , has been identified in linearly polarized starlight for the first time. When the filament stars are omitted from the polarization data set that is evaluated with the merit function $F_{II}(B_i)$, the ISMF direction of B_{POL} is aligned with the direction $\ell = 36.2$, $b = 49.0$ ($\pm 16^\circ$). The direction of B_{POL} is centered $7.6(+14.9, -7.6)$ away from the ISMF direction found from the *IBEX* Ribbon (Table 1). The polarization position angles of the stars that best comply with B_{POL} indicate that the magnetic turbulence of B_{POL} is weak (Section 4.5). Several of the stars that trace B_{POL} are located within ~ 10 pc. B_{POL} is not distinguished by the mean distance of the stars that trace B_{POL} , but those stars tend to show weaker polarizations than average.
4. The local ISMF must be complex because many stars have polarization position angles that trace a magnetic field direction that is different from B_{POL} .
5. B_{POL} must thread the local interstellar clouds. It forms an angle of 76.8 ($+23.5, -27.6$) with the bulk CLIC motion relative to the LSR. This result agrees with previous findings and is consistent with a model where the CLIC is associated with an evolved rim of the Loop I superbubble.
6. The velocities of the 15 CLIC clouds defined by Redfield & Linsky (2008) have been converted into the LSR; those LSR velocities increase as the angle between the LSR velocity and B_{POL} increases. This suggests that B_{POL} orders the kinematics of the local ISM. One possible scenario is that the polarized dust bridge extending from the heliosphere to the North Polar Spur region represents dust and the magnetic fields swept up by the large-scale expansion of the Loop I superbubble.
7. The polarizations of three stars within 20 pc have been compared with hydrogen column densities. Values of $E(B - V)$ were estimated from $N(H^0)$ and then compared with polarization strengths (Section 5.4). The resulting ratios $P\%/E(B - V)$ are consistent with the results of Fosalba et al. (2002) that find an upturn in polarization strengths for low-extinction stars, although uncertainties are large.
8. The polarization data indicate that B_{POL} , which coincides with B_{IBEX} , extends to the edge of the region that was tested by BICEP2 for the B-mode polarization of the CMB. Polarizations of up to 0.2% inside of the BICEP2 field are found, corresponding to a color excess of $E(B - V) \geq 0.028$ mag. Data on starlight reddening give a larger color excess $E(B - V) > 0.2$ mag in the BICEP2 field, corresponding to an optical extinction $A_V > 0.6$ mag.

The only nearby interstellar cloud where the relation between the gas and dust is clearly established is the LIC, where multiple spacecraft have measured UV LIC absorption

lines and the ISMF direction has been found from heliosphere models and the *IBEX* Ribbon. Achieving a similar understanding of the relation between the local ISMF traced by the polarization data and interstellar clouds will require UV studies of the interstellar absorption lines toward the same stars for which high-quality polarization data are available. Only then will a full understanding of the relation between the ISMF that shapes the heliosphere and the magnetic field that is associated with interstellar clouds in the solar vicinity be possible.

This research has been partly supported by the NASA Explorer program through support for the *IBEX* mission, and by the European Research Council Advanced Grant HotMol (ERC-2011-AdG 291659). P. Frisch would like to thank Stephen Case for pointing out the first study of the solar apex motion in Herschel (1783).

APPENDIX A STARS WITH POLARIZATIONS THAT BEST CONFORM TO B_{POL}

The 29 stars with $P/\Delta P \geq 2.0$ that belong to the third of the sample with polarization position angles that best match B_{POL} (see Section 4.4) are: HD 11276, HD 90132, HD 90355, HD 91324, HD 112413, HD 117939, HD 126660, HD 127762, HD 130109, HD 150680, HD 161892, HD 169916, HD 173818, HD 177409, HD 177716, HD 184509, HD 185395, HD 187642, HD 190248, HD 197989, HD 198149, HD 205478, HD 207129, HD 210027, HD 210049, HD 210418, HD 215696, HD 216435, HD 223889.

APPENDIX B COLOR EXCESS $E(B - V)$

The color excess $E(B - V)$ contours in Figure 11 are based on the photometric and astrometric data for stars brighter than $V = 9$ mag in the Hipparcos catalog (Perryman 1997). Color excess values $E(B - V)$ are calculated using the intrinsic stellar colors as a function of spectral type given by Cox (2000). Poorly defined spectral types are weeded out by only using stars where astrometric distances match photometric distances to within 15%. The uncertainties on the astrometric distances are used to spatially smooth the $E(B - V)$ values over $\pm 13^\circ$ angles in the sky for stars with astrometric distances that overlap. Variable stars are not included in the construction of the $E(B - V)$ maps. Variability is filtered out by excluding Hipparcos data with variabilities that are larger than 0.06 mag. The contour levels of $E(B - V) = 0.01, 0.04, 0.09,$ and 0.17 mag correspond to foreground hydrogen column densities of 19.76, 20.37, 20.72, and 20.99 cm^{-2} for $N(H^0 + 2H_2)/E(B - V) = 5.8 \times 10^{21} \text{ cm}^{-2} \text{ mag}^{-1}$ (Bohlin et al. 1978) providing that negligible amounts of H^+ are present.

APPENDIX C COLUMN DENSITIES, COLOR EXCESS AND POLARIZATION STRENGTHS

This appendix summarizes the relations between hydrogen column densities and polarization strengths as determined from the literature. The discussion in Section 5.4 uses these relations to evaluate whether the polarizing mechanisms in the local ISM are more efficient than in the generic ISM.

The relations between color excess $E(B - V)$ and polarization strengths has been determined both for reddened stars

(Serkowski et al. 1975) and lightly reddened stars (Fosalba et al. 2002). The upper envelope of the plot of color excess $E(B - V)$ versus polarization strength for generic reddened stars within several kpc of the Sun is given by $P_{\%} = 9 E(B - V)$, where $P_{\%}$ is percent polarization (Serkowski et al. 1975, Section 2). The upper envelope of the relation between polarization and color excess is found to be nonlinear for lightly reddened stars, $E(B - V) < 1$ mag, giving the alternate relation $P'_{\%} = 3.5 E(B - V)^{0.8}$ (Equation (3) in Fosalba et al. 2002). The term “upper envelope” indicates the maximum polarization that has been observed as a function of extinction, and therefore by common assumption the maximum allowable polarization for a given level of extinction.

Obtaining the dependence of polarization on hydrogen column densities requires the use of an additional relation between extinction and column density. The *Copernicus* mission studied the absorption lines of nearby stars in the far-UV where the H° Lyman lines and H_2 absorption lines are located (Savage et al. 1977; Bohlin et al. 1978). Observations of H° and H_2 yielded a mean ratio of total neutral hydrogen to color excess of $\langle N(H^{\circ} + 2H_2) \rangle / E(B - V) = 5.8 \times 10^{21} \text{ cm}^{-2} \text{ mag}^{-1}$. *Copernicus* did not directly measure column densities of ionized hydrogen, $N(H^+)$. The ionization corrections needed to obtain total hydrogen column densities obtained from $2H^{\circ} + H_2$ are expected to be less than a few percent for the *Copernicus* stars (Bohlin et al. 1978), nearly all of which are beyond 100 pc and therefore beyond the boundaries of the Local Bubble that is nearly devoid of interstellar dust (Fitzgerald 1968).

Observed polarizations may differ from the relation expected from the upper envelope of the relation between polarization and extinction. We introduce the terms α and α' to evaluate the polarization efficiency of reddened and unreddened sightlines, respectively. Variations in the terms α and α' can result from the presence of several different magnetic field directions foreground to the star, patchy dust distributions, and/or variations in the grain characteristics.

The total hydrogen column density is used as a proxy for extinction because the extinction toward nearby stars is too low to be determined with the standard evaluation of the difference between the attenuation of light in the B and V passbands that creates the color excess $E(B - V)$. Hence a second factor that will influence the evaluation of the efficiency of alignment mechanisms is the fractional ionization of hydrogen. Ionization corrections are implemented through the term $\gamma = N(H^+) / N(H^{\circ})$, where $N(H^+)$ is the column density of ionized hydrogen.

Significant amounts of H_2 are not expected in the local ISM because of high fluxes of far-UV and extreme-UV ionizing radiation (Vallerga 1998; Vallerga & Slavin 1998) and low column densities (Wood et al. 2005). Locally the high EUV fluxes also generate significant amounts of H^+ in the LIC (Slavin & Frisch 2008) and other clouds (Slavin & Frisch 1998; Redfield & Falcon 2008). The term $N(H^{\circ}) + 2N(H_2)$ in (Bohlin et al. 1978) can therefore be replaced by $N(H^{\circ}) + N(H^+) = N(H^{\circ})(1 + \gamma)$ for the very local ISM.

For reddened stars and the mean $N(H)/E(B - V)$ *Copernicus* relation:

$$P_{\%} = \alpha 9 E(B - V) \quad (5)$$

$$C = 1.55 \times 10^{-21} \text{ mag cm}^2 \quad (6)$$

$$P_{\%} = \alpha C (N(H^{\circ}) + N(H^+)) \quad (7)$$

$$\alpha = \frac{P_{\%}}{C N(H^{\circ})(1 + \gamma)}. \quad (8)$$

Low extinction stars have a slightly different ratio of hydrogen column density to $E(B - V)$. Restricting the *Copernicus* data sample to those stars with a small fraction of H_2 , $< 1\%$, provided a sample of the “intercloud medium” where the mean ratio between H and $E(B - V)$ is $\langle N(H^{\circ} + H_2) \rangle / E(B - V) = 5.0 \times 10^{21} \text{ cm}^{-2} \text{ mag}^{-1}$ (Bohlin et al. 1978). For lightly reddened stars and the *Copernicus* relation for the intercloud medium the polarization-extinction measure becomes:

$$P'_{\%} = \alpha' 3.5 E(B - V)^{0.8} \quad (9)$$

$$C' = 1.53 \times 10^{-17} \text{ mag cm}^2 \quad (10)$$

$$P_{\%} = \alpha' C' (N(H^{\circ}) + N(H^+))^{0.8} \quad (11)$$

$$\alpha' = \frac{P_{\%}}{C' N(H^{\circ})^{0.8} (1 + \gamma)^{0.8}} \quad (12)$$

which can be used to estimate both α' and γ for sightlines where H° and H^+ and polarization data are available, where α' is the efficiency of grain alignment in the absence of depolarization effects.

These relations are used to evaluate the polarization efficiency in the local ISM in Section 5.4.

APPENDIX D BULK MOTION OF LOCAL INTERSTELLAR CLOUDS RELATIVE TO THE LSR

Astrometric data collected by the founders of modern astronomy revealed that both the Sun and stars are moving through space (Herschel 1783),¹⁷ and led to the recognition that the Sun encounters interstellar clouds during its journey through space (Shapley 1921). Because both the Sun and interstellar clouds move through space, the Doppler contribution of solar motion to the heliocentric interstellar velocities must be removed for comparisons between kinematically defined clouds and spatially defined objects such as Loop I.

For conversion to the LSR velocity frame, which traces the mean velocity of nearby gravitationally relaxed stars around the galactic center, we use the solar motion relative to the LSR derived by Schönrich et al. (2010). Using data from the Hipparcos spacecraft (Perryman 1997), the Schönrich et al. (2010) results for the U , V , and W solar velocity components correspond to a solar velocity of $V = 18.0 \pm 0.9 \text{ km s}^{-1}$ toward $\ell = 47^{\circ}8 \pm 2^{\circ}9$, $B = 23^{\circ}8 \pm 2^{\circ}0$ (e.g., the solar apex motion). The direction determined by Herschel (1783), based on the nearest and brightest stars, was toward the star λ Her that is located 5° away from this direction.

The bulk motion through space of the nearby interstellar material associated with the CLIC, < 30 pc, been determined from the velocities for interstellar optical and UV absorption

¹⁷ “Now, if the proper motion of the stars in general be once admitted, who can refuse to allow that our sun, with all its planets and comets, that is, the solar system, is no less liable to such a general agitation as we find to obtain among all the rest of the celestial bodies. Admitting this for granted, the greatest difficulty will be how to discern the proper motion of the sun between so many other (and variously compounded) motions of the stars. This is an arduous task indeed, which we must not hope to see accomplished in a little time; but we are not to be discouraged from the attempt. Let us, in all events, endeavour to lay a good foundation for those who are to come after us.”

Table 3
Summary of LSR Vectors and Directions

Quantity	LSR Vector Velocity ℓ (deg), b (deg), V (km s ⁻¹)
Vector velocity of solar apex motion ^a	47.8 ± 2.9, 23.8 ± 2.0, 18.0 ± 0.9
Vector velocity of bulk CLIC LSR motion ^b	155.6 ± 13.4, 7.0 ± 9.0, 17.3 ± 4.9
Vector velocity of bulk LIC LSR motion ^c	141.1 ± 5.9, 2.4 ± 4.2, 17.2 ± 1.9

Notes.

^a Based on the U , V , W components of the solar apex motion in Schönrich et al. (2010).

^b Based on the heliocentric velocity vector of the CLIC derived in Frisch et al. (2002), with the additional assumption that uncertainties on the longitude and latitude of the vector are 2° each.

^c This LSR velocity for the LIC is based on the heliocentric velocity derived for the flow of interstellar He^o through the heliosphere that compared in situ *IBEX-LO* He^o data with multivariate simulations of the particle trajectories (Schwadron et al. 2015).

lines, as well as the flow of interstellar dust through the heliosphere. Observations of interstellar absorption lines in 96 stars sampling the nearby ISM have been used to determine the bulk flow of nearby ISM through space for the assumption that the material flows as a rigid-body (Frisch et al. 2002), yielding the heliocentric flow velocity of 28.1 ± 4.6 km s⁻¹ toward $\ell, b = 192^\circ.4, -11^\circ.6$. Uncertainties on the longitude or latitude were not originally provided, so for the purposes of evaluating the motion of the CLIC relative to the LSR, uncertainties of 2° each are adopted for ℓ and b .

The heliocentric velocity of the CLIC, based on the bulk motion of the CLIC in Frisch et al. (2002), is given in Table 3. The LIC LSR velocity in Table 3 is based on the *IBEX* He^o velocity in Schwadron et al. (2015b).

REFERENCES

Abbasi, R., Abdou, Y., Abu-Zayyad, T., et al. 2011, *ApJ*, 740, 16
 Abdo, A. A., Allen, B. T., Aune, T., et al. 2009, *ApJ*, 698, 2121
 Ade, P. A. R. & the BICEP2 team 2014, *PhRvL*, 112, 241101
 Andersson, B.-G. 2015, in *Astrophysics and Space Science Library* 407, ed. A. Lazarian, E. M. de Gouveia Dal Pino & C. Melioli, 59
 Andersson, B.-G., & Potter, S. B. 2006, *ApJL*, 640, L51
 Bailey, J., Kedziora-Chudczer, L., Cotton, D. V., et al. 2015, *MNRAS*, 449, 3064
 Bailey, J., Lucas, P. W., & Hough, J. H. 2010, *MNRAS*, 405, 2570
 Berdyugin, A., Piirola, V., & Teerikorpi, P. 2014, *A&A*, 561, A24
 Bohlin, R. C., Savage, B. D., & Drake, J. F. 1978, *ApJ*, 224, 132
 Burlaga, L. F., & Ness, N. F. 2014, *ApJ*, 784, 146
 Cox, A. N. 2000, *Allen's Astrophysical Quantities* (New York: AIP), 29
 Crawford, I. A. 2001, *MNRAS*, 327, 841
 Fitzgerald, M. P. 1968, *AJ*, 73, 983
 Fosalba, P., Lazarian, A., Prunet, S., & Tauber, J. A. 2002, *ApJ*, 564, 762
 Frisch, P. C. 1981, *Natur*, 293, 377
 Frisch, P. C. 1993, *ApJ*, 407, 198
 Frisch, P. C. 2010, *ApJ*, 714, 1679
 Frisch, P. C., Andersson, B., Berdyugin, A., et al. 2010a, *ApJ*, 724, 1473
 Frisch, P. C., Andersson, B., Berdyugin, A., et al. 2015a, *ApJ*, 805, 60
 Frisch, P. C., Andersson, B.-G., Berdyugin, A., et al. 2012, *ApJ*, 760, 106
 Frisch, P. C., Berdyugin, A., Piirola, V., et al. 2015b, in *Journal of Physics: 13th Annual Int. Astrophysics Conf. 577, Voyager, IBEX and the Interstellar Medium 012010*
 Frisch, P. C., Bzowski, M., Drews, G., et al. 2015c, *ApJ*, 801, 601
 Frisch, P. C., Dorschner, J. M., Geiss, J., et al. 1999, *ApJ*, 525, 492
 Frisch, P. C., Grodnicki, L., & Welty, D. E. 2002, *ApJ*, 574, 834
 Frisch, P. C., Heerikhuisen, J., Pogorelov, N. V., et al. 2010b, *ApJ*, 719, 1984
 Frisch, P. C., Redfield, S., & Slavin, J. 2011, *ARA&A*, 49, 237

Frisch, P. C., & Schwadron, N. A. 2014, in *ASP Conf. Ser. 484, Outstanding Problems in Heliophysics: From Coronal Heating to the Edge of the Heliosphere*, ed. Q. Hu & G. P. Zank (San Francisco, CA: ASP), 42
 Frisch, P. C., & York, D. G. 1983, *ApJL*, 271, L59
 Frisch, P. C., York, D. G., & Fowler, J. R. 1987, *ApJ*, 320, 842
 Funsten, H. O., Allegrini, F., Crew, G. B., et al. 2009, *Sci*, 326, 964
 Funsten, H. O., DeMajistre, R., Frisch, P. C., et al. 2013, *ApJ*, 776, 30
 Fuselier, S. A., Allegrini, F., Funsten, H. O., et al. 2009, *Sci*, 326, 962
 Gry, C., & Jenkins, E. B. 2014, *A&A*, 567, A58
 Heerikhuisen, J., & Pogorelov, N. V. 2011, *ApJ*, 738, 29
 Heerikhuisen, J., Pogorelov, N. V., Zank, G. P., et al. 2010, *ApJL*, 708, L126
 Heerikhuisen, J., Zirnstein, E. J., Funsten, H. O., et al. 2014, *ApJ*, 784, 73
 Heiles, C. 2000, *AJ*, 119, 923
 Herschel, W. E. F. R. S. 1783, *Phil. Trans. R. Soc. Lond.*, 73, 247
 Hoang, T., & Lazarian, A. 2014, *MNRAS*, 438, 680
 Isenberg, P. A. 2014, *ApJ*, 787, 76
 Jones, A. P., Tielsens, A. G. G. M., Hollenbach, D. J., & McKee, C. F. 1994, *ApJ*, 433, 797
 Kim, S.-H., & Martin, P. G. 1994, *ApJ*, 431, 783
 Krueger, H., Strub, P., Sterken, V. J., & Grün, E. 2015, *ApJ*, 812, 139
 Landgraf, M., Baggaley, W. J., Grün, E., Krüger, H., & Linkert, G. 2000, *JGR*, 105, 10343
 Linsky, J. L., Rickett, B. J., & Redfield, S. 2008, *ApJ*, 675, 413
 Livadiotis, G., & McComas, D. J. 2012, *ApJ*, 749, 11
 Mathis, J. S. 1979, *ApJ*, 232, 747
 McComas, D. J., Allegrini, F., Bochsler, P., et al. 2009, *Sci*, 326, 959
 McComas, D. J., Bzowski, M., Frisch, P. C., et al. 2015, *ApJ*, 801, 28
 McComas, D. J., Lewis, W. S., & Schwadron, N. A. 2014, *RvGeo*, 52, 118
 Munch, G., & Unsold, A. 1962, *ApJ*, 135, 711
 Nagashima, K., Fujimoto, K., & Jacklyn, R. M. 1998, *JGR*, 1031, 17429
 Naghizadeh-Khouei, J., & Clarke, D. 1993, *A&A*, 274, 968
 Pereyra, A., & Magalhães, A. M. 2007, *ApJ*, 662, 1014
 Perryman, M. A. C. 1997, *A&A*, 323, L49
 Piirola, V. 1977, *A&AS*, 30, 213
 Piirola, V., Berdyugin, A., & Berdyugina, S. 2014, *Proc. SPIE*, 9147, 91478
 Ratkiewicz, R., Strumik, M., & Grygorczuk, J. 2012, *ApJ*, 756, 3
 Redfield, S., & Falcon, R. E. 2008, *ApJ*, 683, 207
 Redfield, S., & Linsky, J. L. 2008, *ApJ*, 673, 283
 Salvati, M. 2010, *A&A*, 513, A28
 Santos, F. P., Corradi, W., & Reis, W. 2011, *ApJ*, 728, 104
 Savage, B. D., Bohlin, R. C., Drake, J. F., & Budich, W. 1977, *ApJ*, 216, 291
 Schönrich, R., Binney, J., & Dehnen, W. 2010, *MNRAS*, 403, 1829
 Schwadron, N. A., Adams, F. C., Christian, E. R., et al. 2014, *Sci*, 343, 988
 Schwadron, N. A., Allegrini, F., Bzowski, M., et al. 2011, *ApJ*, 731, 56
 Schwadron, N. A., Bzowski, M., Crew, G. B., et al. *Sci*, 326, 966
 Schwadron, N. A., & McComas, D. J. 2013, *ApJ*, 764, 92
 Schwadron, N. A., Möbius, E., & Leonard, T. 2015b, *ApJS*, 220, 25
 Schwadron, N. A., Frisch, P., Jokipii, J. R., et al. 2015a, *ASTRP*, 2, 9
 Serkowski, K., Mathewson, D. S., & Ford, V. L. 1975, *ApJ*, 196, 261
 Shapley, H. 1921, *JG*, 29, 136
 Slavin, J. D., & Frisch, P. C. 1998, in *Proc. IAU Colloquium 166, The Local Bubble and Beyond*, ed. D. Breitschwerdt, M. J. Freyberg, & J. Truemper (Berlin: Springer-Verlag), 305
 Slavin, J. D., & Frisch, P. C. 2008, *A&A*, 491, 53
 Sterken, V. J., Strub, P., Krüger, H., von Steiger, R., & Frisch, P. 2015, *ApJ*, 812, 141
 Tibet Asy Collaboration, Amenomori, M., Bi, X. J., et al. 2011, *AdSpR*, 47, 629
 Tinbergen, J. 1982, *A&A*, 105, 53
 Vallerga, J. 1998, *ApJ*, 497, 921
 Vallerga, J., & Slavin, J. 1998, in *Proc. IAU Colloquium 166, The Local Bubble and Beyond*, ed. D. Breitschwerdt, M. J. Freyberg, & J. Truemper (Berlin: Springer-Verlag), 79
 Vergely, J., Valette, B., Lallement, R., & Raimond, S. 2010, *A&A*, 518, A31+
 Vermetto, S., Guglielmo, Z., Zhang, J. L. & for the ARGO-YBJ Collaboration 2009, arXiv:0907.4615
 Wiktorowicz, S. J., & Nofi, L. A. 2015, *ApJL*, 800, L1
 Wiktorowicz, S. J., Nofi, L. A., Jontof-Hutter, D., et al. 2015, arXiv:1507.03588
 Wisniewski, J. P., Bjorkman, K. S., Magalhães, A. M., et al. 2007, *ApJ*, 671, 2040
 Wolleben, M. 2007, *ApJ*, 664, 349
 Wood, B., Redfield, S., Linsky, J., Müller, H.-R., & Zank, G. 2005, *ApJS*, 159, 118
 Wood, B. E., Redfield, S., Linsky, J. L., & Sahu, M. S. 2002, *ApJ*, 581, 1168